

AGU Advances

RESEARCH ARTICLE

10.1029/2021AV000487

This article is a companion to Codilean and Sadler (2021), <https://doi.org/10.1029/2021AV000539>.

Key Points:

- A 6-Myr-long record of Himalayan erosion rates are measured based on ^{10}Be concentrations in foreland basin sediments
- Erosion rates varied quasi-cyclically with a periodicity of 1 Myr and gradually increased toward the present

Supporting Information:

Supporting Information may be found in the online version of this article.

Correspondence to:

S. K. Mandal,
sanjaykm@iiserkol.ac.in

Citation:

Mandal, S. K., Scherler, D., & Wittmann, H. (2021). Tectonic accretion controls erosional cyclicity in the Himalaya. *AGU Advances*, 2, e2021AV000487.
<https://doi.org/10.1029/2021AV000487>

Received 12 MAY 2021

Accepted 26 JUL 2021

Peer Review The peer review history for this article is available as a PDF in the Supporting Information.

Author Contributions:

Conceptualization: Sanjay Kumar Mandal, Dirk Scherler
Data curation: Sanjay Kumar Mandal
Formal analysis: Sanjay Kumar Mandal, Dirk Scherler
Writing – review & editing: Sanjay Kumar Mandal, Dirk Scherler, Hella Wittmann

© 2021. The Authors.

This is an open access article under the terms of the [Creative Commons Attribution-NonCommercial-NoDerivs License](#), which permits use and distribution in any medium, provided the original work is properly cited, the use is non-commercial and no modifications or adaptations are made.

Tectonic Accretion Controls Erosional Cyclicity in the Himalaya

Sanjay Kumar Mandal^{1,2} , Dirk Scherler^{3,4} , and Hella Wittmann³ 

¹Department of Earth Sciences, Indian Institute of Science Education and Research Kolkata, Nadia, India, ²Centre for Climate and Environmental Studies, Indian Institute of Science Education and Research Kolkata, Nadia, India, ³Earth Surface Geochemistry, GFZ German Research Centre for Geosciences, Potsdam, Germany, ⁴Institute of Geological Sciences, Freie Universität Berlin, Berlin, Germany

Abstract The evolution of Earth's climate over geological timescales is linked to surface erosion via weathering of silicate minerals and burial of organic carbon. However, methodological difficulties in reconstructing erosion rates through time and feedbacks among tectonics, climate, and erosion spurred an ongoing debate on mountain erosion sensitivity to tectonic and climate forcing. At the heart of this debate is the question of whether late Cenozoic climate cooling has increased global erosion rates or not. The Himalaya plays a prominent role in this debate as its erosion produces a large fraction of global sediments delivered to ocean basins. We report a 6-Myr-long record of ^{10}Be -derived erosion rates from the north-western Himalaya, which indicates that erosion rates in this region varied quasi-cyclically with a period of ~1 Myr and increased gradually toward the present. We hypothesize that the observed pattern of erosion rates occurred in response to the tectonic growth of the Himalaya by punctuated basal and frontal accretion of rocks from the underthrusting Indian plate and concomitant changes in topography. In this scenario, basal accretion episodically changes rock-uplift patterns, which brings landscapes out of equilibrium and results in quasi-cyclic variations in erosion rates. We used numerical landscape evolution simulations to demonstrate that this hypothesis is physically plausible. We attribute the long-term increase in erosion rates to the erosional response of topography due to frequent basal accretion relative to frontal accretion. Because tectonic accretion processes are inherent to collisional orogenesis, they likely confound climatic interpretations of erosion rate histories.

Plain Language Summary The Earth's climate has been cooling during the last ~15 million years and started fluctuating between cold and warm periods since ~2–3 million years ago. Many researchers think that these long-term climatic changes were accompanied by changes in continental erosion. However, quantifying erosion rates in the geological past is challenging, and previous studies reached contrasting conclusions. In this study, we quantified erosion rates in the north-western Indian Himalaya over the past 6 million years by measuring the concentration of Beryllium-10 (^{10}Be) in foreland basin sediments. The radioactive element ^{10}Be is produced by cosmic rays in minerals at the Earth's surface, and its abundance indicates erosion rates. Our reconstructed erosion rates show a quasi-cyclic pattern with a periodicity of ~1 million year and a gradual increase toward the present. We suggest that both patterns—cyclicity and gradual increase—are unrelated to climatic changes. Instead, we propose that the growth of the Himalaya by repeatedly scraping off rocks from the Indian plate, resulted in changes of its topography that were accompanied by changes in erosion rates. Our study is amongst the first that documents cyclic erosion rates that could plausibly be linked to the tectonic evolution of orogenic wedges, and may thus change the way erosion histories are interpreted globally.

1. Introduction

The collision between the Indian and Eurasian plates has been ongoing since ~54 Ma (Najman et al., 2017) and formed the ~2500-km long Himalaya at the southern margin of the Tibetan Plateau (Figure 1a). Erosion of the Himalaya accounts for a large fraction of the sediment and dissolved material delivered to the oceans (Milliman & Farnsworth, 2011). Himalayan erosion is therefore considered a key figure in the evolution of Earth's climate over geological timescales by the burial of organic carbon (Galy et al., 2007) and sequestration of atmospheric CO_2 during silicate weathering (Raymo & Ruddiman, 1992). Because most

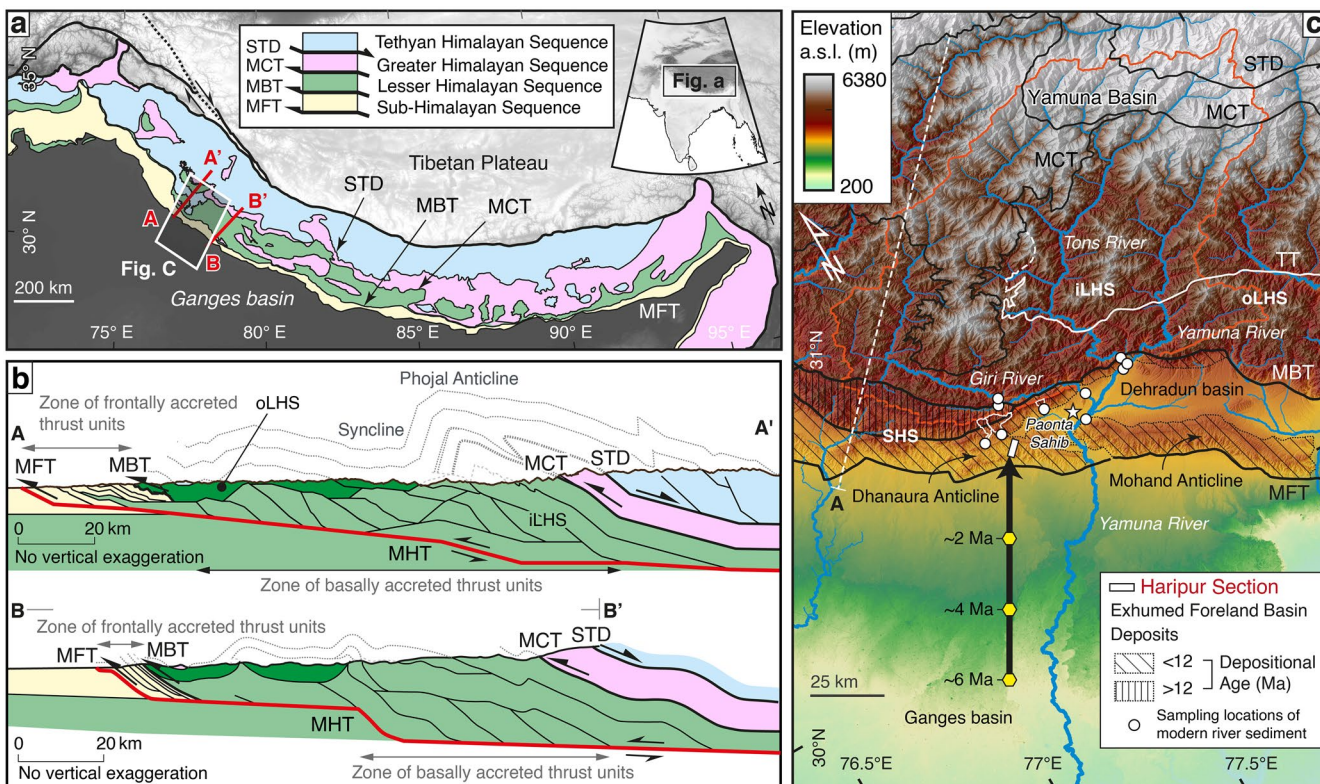


Figure 1. Simplified geology of the Himalaya, structural cross sections, and topography of the study area. (a) Geologic overview map of the Himalaya (location in inset) showing the main tectonic units. MBT, Main Boundary Thrust; MCT, Main Central Thrust; MFT, Main Frontal Thrust; STD, South Tibetan Detachment. (b) Balanced structural cross sections along the A-A' and B-B' transects, modified from Srivastava and Mitra (1994) and Webb (2013). MHT, Main Himalayan Thrust. (c) Topographic overview of the study area from a 30-m digital elevation model. Outline of the Yamuna catchment shown by the orange line. Thick white dashed line = location of the cross section line A-A' shown in (a). Note that the north-eastern part of the line is clipped at the figure limit. iLHS, inner Lesser Himalayan Sequence; oLHS, outer Lesser Himalayan Sequence; SHS, Sub-Himalayan Sequence; TT, Tons Thrust. Arrow indicates the past location of the depocenter, assuming a steady convergence rate of $\sim 18 \text{ mm yr}^{-1}$ (Stevens & Avouac, 2015) and that about two-thirds of this convergence rate is accommodated by thrusting of the Indian plate beneath the Himalaya (Avouac, 2015). White circles show the sampling locations of modern river sediments.

erosion processes in the Himalaya are active during the wet summer monsoon season (Gabet et al., 2008), temporal changes in erosion rates are commonly attributed to changes in monsoon intensity (Bookhagen et al., 2005; Clift et al., 2008; Goodbred et al., 2000). For example, the establishment of focused monsoonal precipitation during the early Miocene has been invoked to explain both the style (Beaumont et al., 2001) and the rate (Clift et al., 2008) of exhumation in the Himalaya. However, continuous records of how erosion rates change through time are rare and prone to methodological limitations. Global proxies such as sediment accumulation rates (Peizhen et al., 2001) suffer from drawbacks related to stratigraphic incompleteness (Sadler, 1981), and sediment budgets might be biased by the glacio-eustatic changes that allowed to remobilize previously stored-sediments on continental margins (Romans et al., 2016). In situ thermochronometry-derived exhumation rates (Herman et al., 2013), on the other hand, can suffer from the intermittency of erosional processes when integrating erosion rates over different time scales (Finnegan et al., 2014; Ganti et al., 2016) or from combining data with disparate exhumation histories (Schildgen et al., 2018; Willett et al., 2020).

Cosmogenic nuclides such as in situ-produced ^{10}Be in sedimentary deposits are useful tracers for paleo-erosion rates (e.g., Charreau et al., 2011; Lenard et al., 2020; Oskin et al., 2017; Puchol et al., 2016; Val et al., 2016), provided that the sediment source areas are known and the source catchments are free from glacial cover that complicates the conversion of measured ^{10}Be concentrations to erosion rates (Godard et al., 2012; Kapannusch et al., 2020). Lenard et al. (2020) showed that ^{10}Be concentrations in Bengal Fan sediments averaged over intervals of 0.5–2.5 Myr have been steady since ~ 6 Ma, suggesting stable erosion

rates over this time interval in the Himalaya. However, the $^{26}\text{Al}/^{10}\text{Be}$ ratio in modern sands from the lower Ganges-Brahmaputra River, near the Bay of Bengal, has been found to be significantly lower than their surface-production-rate ratio of 6.75 (Wittmann et al., 2020), indicating that modern, and thus potentially also paleo- ^{10}Be concentrations in Bengal Fan sediments may be biased by decay during transient sediment storage in the Ganges-Brahmaputra plain. Furthermore, the stratigraphic record of the Bengal Fan may contain a spatially and temporally mixed ^{10}Be signal, which is unlikely to document erosion rate variations unless they occur over several millions of years (e.g., Romans et al., 2016).

Instead, the sedimentary archive of a proximal foreland basin that is intimately linked to the eroding hinterland catchments by a simple sediment routing system allows reconstructing a history of source area erosion rather straightforwardly (e.g., Charreau et al., 2011; Puchol et al., 2016). To directly gauge the sensitivity of Himalayan erosion to past changes in climate and tectonics, we reconstructed erosion rates during the past \sim 6 Myr using late Miocene to Pleistocene foreland basin sediments from north-western India (hereafter referred to as Siwaliks). The studied Siwalik section is particularly well suited for such a task for several reasons. First, a previous provenance study has reconstructed the sediment source areas (S. K. Mandal et al., 2018). Second, the sedimentary succession was previously dated using magnetostratigraphy (Sangode et al., 1996), which provides a temporal framework for estimating paleoerosion rates using ^{10}Be . Third, Pleistocene glaciation in the hinterland of our study area was limited (Kapannusch et al., 2020; Scherler et al., 2010), which makes the foreland deposits suitable for determining paleoerosion rates using ^{10}Be . Fourth, previous work by Wittmann et al. (2020) showed that the $^{26}\text{Al}/^{10}\text{Be}$ ratios in sands from the lower Ganges catchment are close to their surface-production-rate ratio, indicating negligible transient storage of sediment in floodplains. In contrast, a low $^{26}\text{Al}/^{10}\text{Be}$ ratio, indicating significant sediment storage in the floodplains, is found only after the confluence of the Ganga and the Brahmaputra. Hence, we assume that the decay of ^{10}Be related to the incorporation of previously buried floodplain sediment that may bias paleo- ^{10}Be records is unlikely for our study section because sediments were deposited far upstream in the upper Ganges basin. Fifth, the growth of the Himalaya through frontal accretion (Figure 1b) has incorporated the Siwalik stratigraphy into the fold-and-thrust belt, resulting in their uplift and exhumation since the mid-Pleistocene (Barnes et al., 2011), which in turn provides direct access to the Siwalik sediments for sampling.

Here, we estimated the paleoerosion rates by measuring the concentration of in situ-produced cosmogenic ^{10}Be in quartz of 41 sandstone samples collected along the Haripur section, which is exposed in the Dhanaura anticline (Figure 1c). The ^{10}Be concentration of exhumed older foreland basin sediment integrates its entire exposure history: exhumation via erosion through the near-surface, sediment transfer by rivers to the foreland, near-surface residence during progressive burial as a sedimentary deposit, and eventual re-exposure following basin inversion (e.g., Charreau et al., 2011; Oskin et al., 2017; Puchol et al., 2016). In the following, we first reconstructed the ^{10}Be concentrations acquired during hillslope erosion in the past by sequentially constraining the ^{10}Be production during these multiple stages of production and accounting for the ^{10}Be decay using magnetostratigraphy-derived ages of sediment deposition. We supplement the paleoerosion rate data with 10 modern catchment-average erosion rate estimates using ^{10}Be abundances in sands from the Yamuna trunk stream and tributaries near the mountain front (Figure 1c). Based on our new data, we hypothesize that punctuated tectonic accretion—the common mode of mountainous growth at continental collisional zones—may be a fundamental cause for late Cenozoic variations in Himalayan erosion rates that we illustrate using a simple numerical landscape evolution model.

2. Background

2.1. Structural Evolution of the Himalaya

The Haripur section is exposed along the Somb River about 20 km west of the town of Paonta Sahib at the front of the north-western Indian Himalaya (30.4°N , 77.4°E ; Figure 1c). As elsewhere throughout the Himalaya, the tectonic architecture in the study area consists of a series of thrust sheets that are separated by northward dipping faults, and broad juxtaposed synforms and antiforms (Srivastava & Mitra, 1994; Webb, 2013; Webb et al., 2011) (Figures 1a and 1b). The major thrust faults root into the Main Himalayan

Thrust (MHT; Figure 1b) (Avouac, 2015)—the décollement along which the Indian plate thrusts beneath the Himalaya at a rate of $\sim 20 \text{ mm yr}^{-1}$ (Lavé & Avouac, 2000). The older hinterland fold-and-thrust belt consists of Tethyan Himalayan, Greater Himalayan, and Lesser Himalayan Sequences (LHSs). The younger foreland fold-and-thrust belt consists of Sub-Himalayan Sequences (SHSs, Figures 1a and 1b).

The structurally higher, low-grade metamorphic Tethyan Himalayan sequence is separated by the north-dipping South Tibetan Detachment from the Himalayan metamorphic core that constitutes the Greater Himalayan Sequence (GHS). The Main Central Thrust zone comprises a series of thrust structures that separate the GHS from low-grade metamorphic rocks constituting the LHS. The Tons Thrust further separates the LHS into the Neoproterozoic-Cambrian outer-LHS in the hanging wall and the Paleoproterozoic inner-LHS in the footwall (Figure 1c). The LHS comprises broad juxtaposed synforms and antiforms, with the latter typically assumed to be cored by a duplex structure (Srivastava & Mitra, 1994; Webb, 2013) (Figure 1b). Geological evidence illuminates the development of Lesser Himalayan duplex structures along the 1,500-km length of the Himalaya, although with considerable variations in geometry, stratigraphic position, and the total amount of shortening (e.g., Bhattacharyya & Mitra, 2009; DeCelles et al., 2016; Robinson & Martin, 2014; Srivastava & Mitra, 1994; Webb, 2013). The LHS accounts for $\sim 30\%-55\%$ of total shortening in the Himalayan fold-and-thrust belt, with the duplex structures generally accomplishing a significant portion of this shortening. For example, in the Garhwal Himalaya (section B-B' in Figure 1b), it has been estimated that the LHS accounts for 31% of the total Himalayan shortening of 525 km, and $\sim 20\%$ of this LHS shortening has been accommodated by duplex structures (Srivastava & Mitra, 1994).

The development of Lesser Himalayan duplex structures has been inferred to occur by the southward migration of a more localized steeper ramp segment—in contrast to one that is much larger and shallowly dipping—along the MHT (Herman et al., 2010; Mendoza et al., 2019; Mercier et al., 2017; Zilio et al., 2020). As the steeper ramp propagates southward, more thrust sheets (formed between successive ramps) are incorporated into the Lesser Himalayan duplex (Figure 1b). A similar tectonic configuration along the MHT has recently been inferred in central Nepal from the spatial distribution of aftershocks following the 2015 Mw 7.8 Gorkha earthquake (Mendoza et al., 2019). The surface expression of the growth of the duplex stack at depth has been manifested by the formation of large foreland-verging thrust-cored anticlines. A local example of this is the partly eroded Phojal anticline, north-west of our study area (section A-A' in Figure 1b), where previous work inferred that basal accretion of the inner-LHS beneath the MCT began during the late Miocene (Colleps et al., 2019; Webb, 2013).

The Main Boundary Thrust (MBT) places the outer-LHS rocks on the Cenozoic foreland basin deposits that comprise the SHS (Figures 1c and 2). The growth of the Himalaya through frontal accretion has incorporated the SHS stratigraphy into the foreland fold-and-thrust belt and formed a hinterland-dipping imbricate zone (Avouac, 2015; Mishra & Mukhopadhyay, 2012) (Figure 2). In the study area, the Sub-Himalayan imbricate zone is comprised of $<12 \text{ Ma}$ Siwalik Group and the older ($>12 \text{ Ma}$) pre-Siwalik Group rocks (Najman et al., 2004). Thin-skinned tectonics associated with the Main Frontal Thrust (MFT)—the youngest, most active, and southernmost thrust system in the Himalaya—has incorporated the Siwalik stratigraphy into the orogenic wedge and formed the Siwalik hills, the southernmost topographic expression of the Himalaya (Figure 2). In the nearby Mohand anticline (Figure 1c), a radiocarbon-dated fluvial terrace constrains the slip rate on the MFT during the Holocene to be $13.8 \pm 3.6 \text{ mm yr}^{-1}$ (Wesnousky et al., 1999), which is $\sim 75 (\pm 20)\%$ of the $18.5 \pm 1.8 \text{ mm yr}^{-1}$ convergence between India and south Tibet in our study area (Stevens & Avouac, 2015).

Most researchers agree that the first phase of the Himalayan orogeny began with the India-Eurasia collision and mainly comprised folding and thrusting of the THS over the Indian continental lithosphere until 30–25 Ma (e.g., Ratschbacher et al., 1994; Webb et al., 2011). During the second, late Oligocene-early Miocene phase, metamorphosed GHS rocks were transported southward along the MCT (e.g., Catlos et al., 2001; Kohn, 2014; Vannay et al., 2004). During the still ongoing third phase, further shortening produced the Lesser Himalayan duplex by basal accretion and the Sub-Himalayan fold-and-thrust belt by frontal accretion (e.g., Mishra & Mukhopadhyay, 2012; Srivastava & Mitra, 1994; Webb, 2013) (Figure 3). In the north-western Himalaya, basal accretion is active since at least 10 Ma, whereas frontal accretion affects foreland basin strata since $\sim 5 \text{ Ma}$ (Colleps et al., 2019; S. K. Mandal et al., 2018).

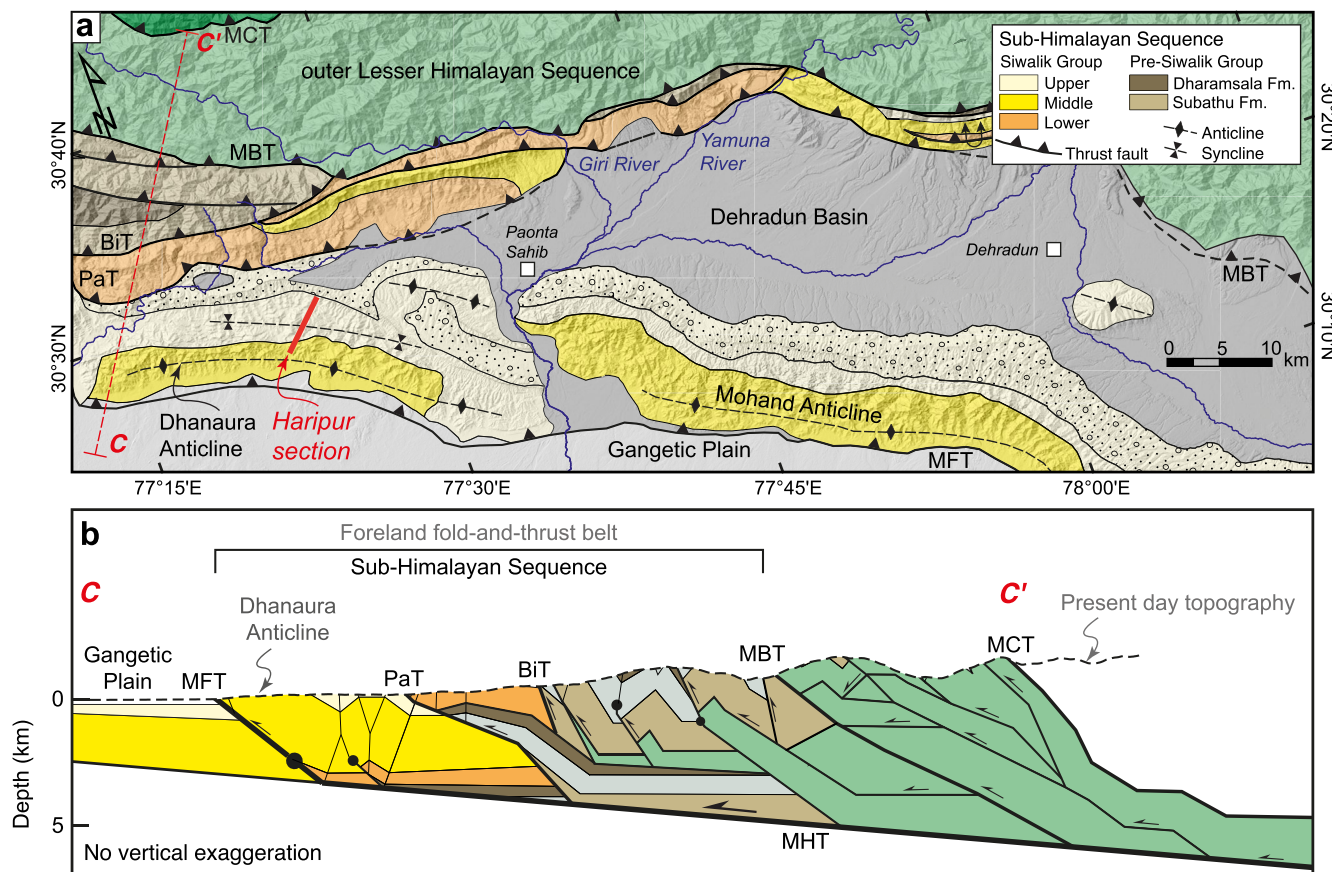


Figure 2. Geology of the Sub-Himalaya. (a) Enlargement of the geology of the Sub-Himalaya in the study area. Thick red line = location of Haripur section; C-C' = location of the balanced structural cross section shown in (b). (b) Balanced structural cross section along the transect C-C' modified after Mishra and Mukhopadhyay (2012). BiT, Bilaspur Thrust; MBT, Main Boundary Thrust; MCT, Main Central Thrust; MFT, Main Frontal Thrust; PaT, Paonta Thrust.

2.2. Sedimentology of the Siwalik Succession Along the Haripur Section

A detailed sedimentological account of the Haripur section has been provided by Sangode et al. (1996) and Kumar et al. (1999), and only summary descriptions and interpretations are presented below.

The lower ~500 m of the section is composed predominantly of thickly bedded (20–40 m), multistorey gray sandstones with minor intervening overbank mudstones (Figure S1) that have been interpreted as amalgamated braided channel fills. The large-scale (up to 2 m) cross bed sets and the low variability in paleoflow toward the southeast indicate sediment deposition by a low sinuosity trunk stream, presumably comparable to the modern Yamuna River (Kumar et al., 1999).

Between ~500 and ~900 m, the rocks are dominated by fine- to medium-grained, gray multistoried sandstones with minor buff-colored ribbon sandstones and a relatively higher proportion of overbank mudstones (Figure S1). Paleoflow within this interval is highly variable, toward the southeast to southwest. The presence of lateral accretion surfaces and channel plug deposits in the sandstone bodies, and the concomitant increase of finer-grained overbank deposits and matured paleosols, suggest deposition by trunk meander streams in a rapidly subsiding depositional sink (Kumar et al., 1999).

The succession between ~900 and 2,100 m is composed of fine- to coarse-grained, brown/buff ribbon sandstones, and thick gray sandstones that are interbedded with thick brown/buff-colored mudstones (Figure S1). These facies are characteristic of an unconfined braided river with the insertion of local streams on an alluvial fan. In these units, paleocurrent indicators suggest that the buff sandstones were deposited by streams draining to the southeast. In contrast, the gray sandstones were deposited by southwest flowing rivers (Kumar et al., 1999). The gray sandstones often contain quartzite and gneiss pebbles (Figure S2).

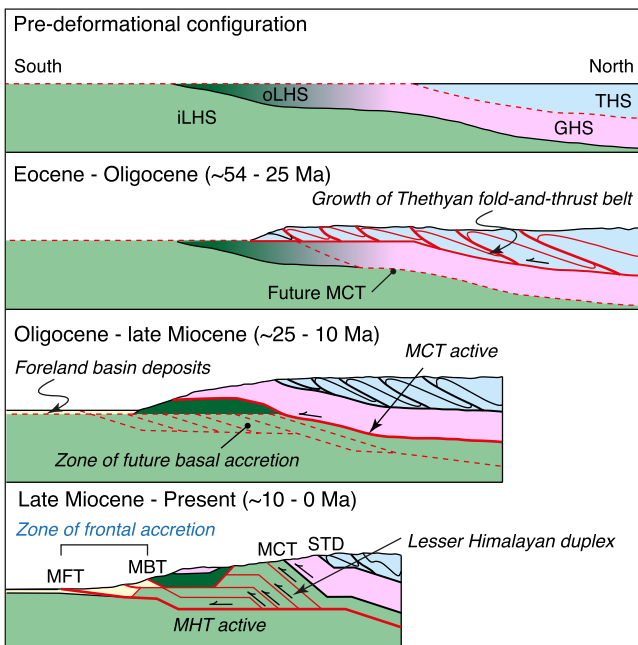


Figure 3. Schematic model of the structural evolution of north-western Indian Himalaya (modified from Colleps et al., 2018). This scheme is based mainly on observations along sections across the Kumaun-Garhwal Himalaya of north-western India. MBT, Main Boundary Thrust; MCT, Main Central Thrust; MFT, Main Frontal Thrust; STD, South Tibetan Detachment.

of the Gangetic plain—was most likely dominated by the Yamuna River, which is consistent with the deposition of gray multistorey sandstone complexes by a south-southwesterly-flowing large transverse river system (Section 2.2). Furthermore, the published $^{87}\text{Sr}/^{86}\text{Sr}$ and $\varepsilon\text{Nd}(0)$ values for sediment sampled from the multistorey gray sandstones (Figure 5) fall between the compositional space of the GHS and inner-LHS end-members and overlaps broadly with isotopic composition of present-day Yamuna River sediment, which indicates sediment supply from the hinterland of the Yamuna catchment (S. K. Mandal et al., 2018). As the depocenter moved closer to the mountain front with time, the likelihood of intermittent sediment deposition by local piedmont rivers increased, as the main Yamuna River flowed away from the depocenter (where the Haripur section is located). We infer that the buff ribbon sandstones were deposited by the southeasterly flowing laterally confined piedmont river system during this time (Kumar et al., 1999). The apparent eastward growth of frontal topography along the MBT might have shifted the confluence of the Giri and Yamuna rivers toward the Dehradun basin (Figure 2a), and thereby forced the Yamuna megafan to encroach gradually to the east. As a consequence, local piedmont streams that drain the foreland fold-and-thrust belt might have supplied sediment intermittently to the depositional sink as the Yamuna River swept across the megafan (S. K. Mandal et al., 2018). Since about 5 Ma, the intermittently occurring buff ribbon sandstones in association with the thick multistorey gray sandstones in the stratigraphy and the frequent change in the depositional milieu from channel to floodplain (Section 2.2) support this assertion (Kumar et al., 1999; Sangode et al., 1996).

Sediment deposition by piedmont rivers implies the possibility that sands were recycled from older foreland basin stratigraphy (S. K. Mandal et al., 2018). Frontally accreted older stratigraphic units that could act as sediment sources over the past ~5 Myr, comprise the >12 Ma pre-Siwalik Group and the <12 Ma lower Siwalik units (Figure 2). As the pre-Siwalik Group (Dharamsala and Subathu formations) mainly consists of fine-grained clastic sediments from the distal foredeep (Najman et al., 2004), it is unlikely to be the source for the coarse-grained quartz sand. In contrast, the <12 Ma lower Siwalik sandstones that are exposed in the hanging wall of the Paonta Thrust, to the north of our study section (Figure 2a), could be a potential source. Unfortunately, these rocks carry a similar isotopic fingerprint as the GHS in the hinterland

which are also found in the hinterland-draining modern Yamuna River. This resemblance in gravel composition indicates deposition of the gray sandstone units by a comparable river system.

Above ~2,100 m, the section is comprised mainly of conglomerates, fine- to medium-grained brown/buff sandstones and siltstones, and thick brown mudstones (Figure 4). The conglomerates are composed predominantly of poorly sorted reworked sandstone clasts (Figure S2). Sedimentary facies point to deposition in the proximal part of the alluvial fan. Paleocurrent indicators point to mainly southward flow directions, with variations to southwest and southeast (Kumar et al., 1999).

2.3. Sediment Provenance

Reconstructing paleo-erosion rates from ^{10}Be concentrations in foreland basin sediments requires that sediment source areas are known, because ^{10}Be production rates are elevation-dependent and source areas might have changed over time. Thrusting of the Indian plate beneath the Himalaya and concomitant crustal shortening implies that over the past 6 Myr, the depocenter has moved closer to the mountain front with time (Lyon-Caen & Molnar, 1985; Mugnier & Huyghe, 2006). The progressive upsection coarsening of sediments (i.e., an upward gradation from distal to more proximal facies) supports this supposition. Assuming that the convergence rate between India and Tibet remained steady at $\sim 18 \text{ mm yr}^{-1}$ (Stevens & Avouac, 2015) and that underthrusting accommodates about two-thirds of this convergence rate (Avouac, 2015; Herman et al., 2010), the depositional sink was ~70 km away from its current location at ~6 Ma (Figure 1c). Sediment deposition at that distal location—based on an analogy with the modern drainage pattern

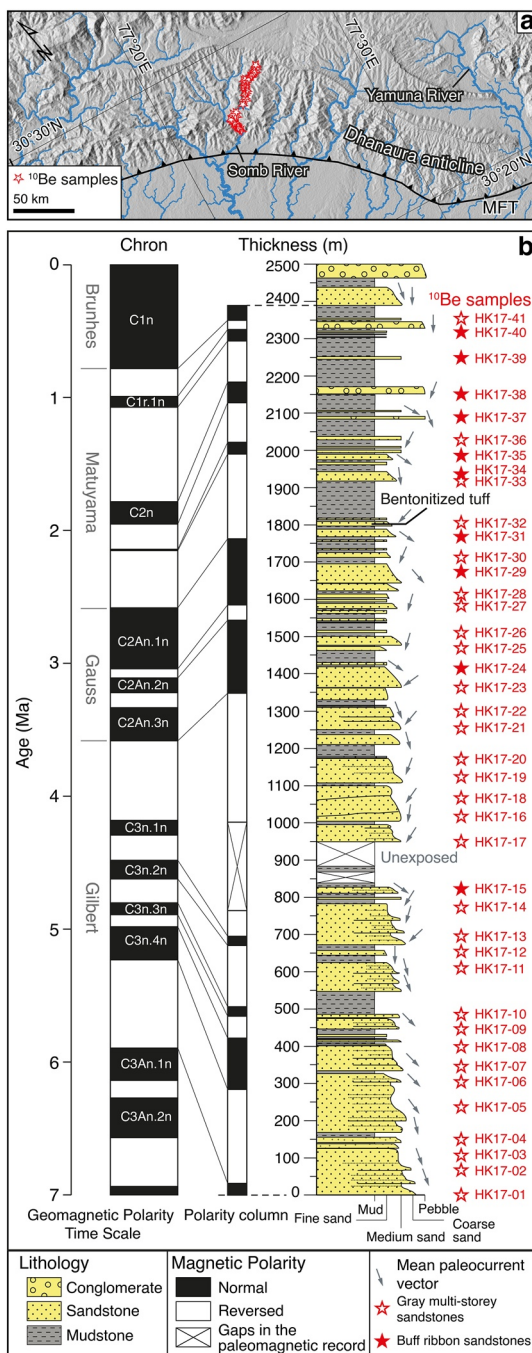


Figure 4. Stratigraphic profile of the Haripur section with ^{10}Be sample locations. (a) Location of the Haripur section and sample collection sites across the Dhanaura anticline. (b) Magnetic polarity column, reported by Sangode et al. (1996), and the best-fit correlation (Data and Methods) with the global magnetic polarity reference scale.

modern Yamuna sediment), the main tributaries of the Yamuna River near the Dehradun basin, and the small streams that drain the frontally accreted lower Siwalik units in the hanging wall of the Paonta Thrust (hereafter referred to as modern piedmont sediment) (Figure 1c).

(Figure 5), which makes it difficult to unambiguously identify sediment recycling from the lower Siwalik units (S. K. Mandal et al., 2018). Nevertheless, the occurrence of reworked sandstone pebbles in conglomerates (Figure S2) since about 2 Ma argues for sediment recycling from the lower Siwalik units. In summary, sedimentology and provenance data of gray multistorey sandstones of the Haripur section point to sediment sourcing from the Yamuna catchment (hereafter referred to as paleo-Yamuna sediment). In contrast, the sedimentology and clast provenance indicate that the material of buff-colored ribbon sandstones was likely shed from the piedmont catchments, possibly in the hanging wall of the Paonta Thrust (hereafter referred to as paleo-piedmont sediment).

3. Materials and Methods

3.1. Sample Collection

To ensure the correct positioning of the ^{10}Be samples in the previously published magnetostratigraphy of the Haripur section (Sangode et al., 1996), we reestimated the stratigraphic thickness with a combination of measuring tape and Bushnell ProX2 laser range finder (accuracy: ± 0.5 m). Our reestimated total stratigraphic thickness differed from the published one by 15 m, which is $<1\%$ deviation. Excellent exposures in the field enabled us to correlate individual units and marker beds with the published stratigraphic column. The sample collection sites were assigned positions in the stratigraphic column (Figure 4) using the thickness measured between the sample sites and the bottom of the section. This helped us to determine the time of sediment deposition using the magnetic polarity column published by Sangode et al. (1996). We carefully selected our sampling sites to ensure low ^{10}Be accumulation due to recent exposure during exhumation of the Siwalik units. We mainly targeted outcrops at the base of tall cliffs that show evidence of recent cliff face rejuvenation by lateral channel migration, undercutting, and collapse. Sand samples were collected either by excavating the soft and friable sandstone bodies at least 60 cm across the exposed cliff faces or from naturally formed caves along the river bank (Figure S3). All sampling sites were selected either a meter away from the bedding plane or in the middle of the thick sand bodies, where we found evidence of incised channel deposits.

We collected 41 sandstone samples along the $\sim 2,400$ -m thick succession of fluvial deposits (Figure 4). Up to the $\sim 1,400$ m level of the section, we collected samples from the medium- to coarse-grained, gray-colored thickly bedded (>5 m) sandstones at a stratigraphic spacing of ~ 50 m. Above $\sim 1,400$ m of the section, the gray-colored sandstone units (the paleo-Yamuna sediment) occur less frequently, and we also collected samples from the $\sim 1\text{--}4$ -m thick, brown/buff-colored fine- to medium-grained sandstones (the paleo-piedmont sediment). To complement the interpretation of paleo-erosion rates, we also collected 10 modern sand samples from the Yamuna mainstream near the mountain front (hereafter referred to as

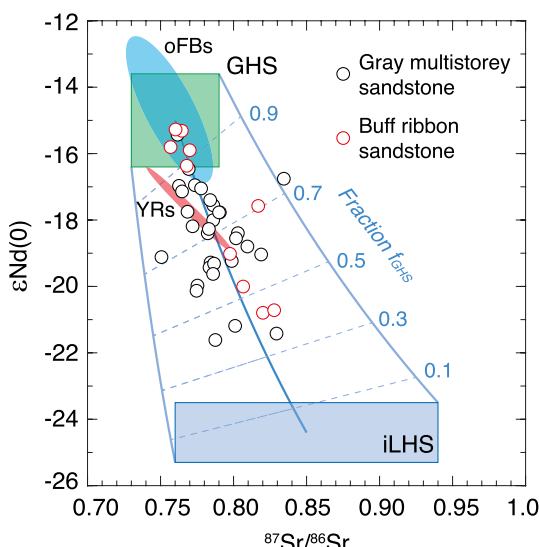


Figure 5. Published Sr-Nd isotopic compositions of sediments from the Haripur section (S. K. Mandal et al., 2018) along with compositional fields of Greater Himalayan Sequence (GHS) and inner Lesser Himalayan Sequence (iLHS). Magenta ellipse (YRs) = published Sr-Nd isotopic composition of the modern Yamuna River sediments near the mountain front (Tripathi et al., 2013). Red ellipse (oFBs) = published Sr-Nd isotopic composition of the late Oligocene to late Miocene older foreland basin sediments (Najman et al., 2000).

3.2. Magnetostratigraphic Age Control

The depositional age of the ^{10}Be samples was constrained using magnetostratigraphy, documented by Sangode et al. (1996). A bentonite tuff horizon interbedded in the Haripur section at $\sim 1,800$ m, and independently dated to ~ 2.5 Ma in the adjoining Ghaggar section (Mehta et al., 1993), enabled correlation of the measured magnetic polarity column to the reference time scale. Notwithstanding, several authors have reported different correlations of the magnetic polarity column of the Haripur section with the geomagnetic polarity timescale (GPTS) (Kumar et al., 1999; Sangode et al., 2001; Sanyal et al., 2004). To eliminate the subjectivity in correlating the published polarity column to the GPTS, we determined a best-fit correlation to the reference scale using the approach proposed by Lallier et al. (2013) and software Cupydon v0.99.0 (retrieved from <http://ring-georessources.univ-lorraine.fr/12-web-site/softwares>), which minimizes local variations in accumulation rate. The minimum cost correlation, shown in Figure 4, dates the section from chron C1n to C3An.1n. Following previous studies (Charreau et al., 2011; Madella et al., 2018), the depositional ages of the samples have been assigned the minimum and maximum ages of the polarity interval to which they belong. In cases where a polarity chron hosts multiple samples, the duration of the chron has been divided for the number of samples included. Accordingly, the sediments analyzed in this study are considered to have been deposited in the foreland basin between 5.98 ± 0.11 Ma and 0.71 ± 0.08 Ma.

3.3. Analytical Procedure

All sandstone samples were crushed and sieved to 250–1,000 μm except samples# HK17-14 and HK17-41 that were sieved to 125–500 μm size fractions before quartz purification. All modern river sediments were

sieved to 250–1,000 μm size fractions. Quartz was separated from the sieved material following standard procedures, including magnetic separation, cleaning in hydrochloric acid, flotation, and three to six sequential leaching steps in diluted hydrofluoric/nitric acid mixtures. Before digestion, the purified quartz was leached in 7 M hydrofluoric acid and aqua regia to eliminate meteoric ^{10}Be . Between ~ 100 and 170 g of pure quartz were dissolved in concentrated hydrofluoric acid after the addition of ~ 150 μg of an in-house ^9Be carrier solution (369.5 ppm). Beryllium was extracted using ion-exchange column chromatography and alkaline precipitation at the Helmholtz Laboratory for the Geochemistry of the Earth Surface at GFZ Potsdam, following established protocols (von Blanckenburg et al., 1996). The $^{10}\text{Be}/^9\text{Be}$ ratios were measured with accelerator mass spectrometry at the University of Cologne (Dewald et al., 2013). The measured $^{10}\text{Be}/^9\text{Be}$ ratios were normalized to the standard KN01-6-2 and KN01-5-3, which have nominal $^{10}\text{Be}/^9\text{Be}$ ratios of 5.35×10^{-13} and 6.32×10^{-12} , respectively, and are consistent with a ^{10}Be half-life of $(1.36 \pm 0.07) \times 10^6$ yr and the 07KNSTD standardization (Nishiizumi et al., 2007). A 6-month average $^{10}\text{Be}/^9\text{Be}$ blank ratio of $(1.62 \pm 1.01 [1\sigma]) \times 10^{-15}$ ($n = 10$), which correspond to 2%–28% of the measured values of paleo-samples, was subtracted for calculating the ^{10}Be concentration in our paleo-sediments. The average blank $^{10}\text{Be}/^9\text{Be}$ ratio was calculated using the four blanks processed alongside the 41 paleo-samples of this study and six blanks processed by other lab users during the time we processed our samples. Using this long-term blank value instead of a single blank ratio for each sample batch ensures both lab background conditions and user- and sample-related contamination issues are adequately reflected in our low- ^{10}Be concentration paleo-samples. For the higher ^{10}Be concentration modern sediments, we subtracted a batch analytical blank $^{10}\text{Be}/^9\text{Be}$ ratio of $(1.57 \pm 0.46) \times 10^{-15}$, which amounts to about 2%–11% of the measured values of modern samples. We propagated the uncertainties of (a) the analytical measurement of the $^{10}\text{Be}/^9\text{Be}$ ratio, (b) the quartz mass, (c) the blank, and (d) the carrier mass to derive ^{10}Be concentrations. The bulk of uncertainty (>75%) is analytic, whereas the remainder is dominated by the blank, especially for the low-concentration paleo-samples.

3.4. Paleoconcentrations of ^{10}Be in Sediments Prior to Burial in the Foreland Basin

^{10}Be is produced within quartz by nuclear reactions with secondary cosmic ray particles. Because production rates decrease exponentially with depth below the Earth's surface, the concentration of ^{10}Be indicates erosion rates of upstream contributing areas when analyzed in modern or ancient river sediments with an integration timescale of typically $10^2\text{--}10^4$ years (von Blanckenburg, 2006). When measured in well-dated foreland basin sediment, ^{10}Be concentrations record erosion rates of the hinterland at the time of their deposition (Charreau et al., 2011; Puchol et al., 2016; Val et al., 2016). However, inferring past erosion rates from ^{10}Be concentrations (C_M) measured in sediment from an exhumed older foreland basin succession is not straightforward, because of the multiple stages of production and decay during hillslope erosion in the past, sediment transfer by rivers to the foreland, progressive burial, and eventual re-exposure following basin inversion (Charreau et al., 2011). Upon erosion of source rocks in a given catchment, the sediment acquired an initial ^{10}Be concentration (C_H) that is inversely proportional to the erosion rate (Bierman & Steig, 1996; Brown et al., 1995; Lal, 1991). When transported from the hillslope to the adjacent foreland basin, the sediment may acquire an additional ^{10}Be component (C_T) that depends on the transit time and intermittent storage within the catchment. When the sediment eventually reached the depositional site, they were gradually buried to great depths, where they remained for millions of years. During this stage, two processes changed their initial ^{10}Be concentrations. First, during burial, the sediments remained partly exposed to cosmic rays and acquired additional ^{10}Be concentrations (C_B) that depend on the sediment accumulation or burial rate (Charreau et al., 2011). Second, during residence in the sub-surface, below the penetration depth of cosmic rays, no additional ^{10}Be accumulated. Instead, the so-far accumulated ^{10}Be (i.e., $C_H + C_T + C_B$) underwent radioactive decay. Finally, during basin inversion, that is, uplift of the foreland deposits as a result of crustal shortening, the previously buried sediment was exhumed to the surface and gradually re-exposed to cosmic rays, which results in the accumulation of an additional ^{10}Be component (C_{Ex}). Therefore, the measured ^{10}Be concentration, C_M , can be described as:

$$C_M = (C_H + C_T + C_B) \cdot e^{-\lambda t} + C_{Ex} \quad (1)$$

where t is the time (yr) of sediment burial before present (i.e., the depositional age of the sediment) and λ is the decay constant of ^{10}Be . Previous studies suggest that transient sediment storage in valleys at the southern front of the Himalaya can be up to 100 kyr, but is rarely longer than 50 kyr (Scherler et al., 2015), which corresponds to <2.5% of radioactive decay prior to burial in the foreland basin. Because this percentage is low and only a fraction of sediment eroded from the Himalaya is likely to be transiently stored at all, we assume that C_T is negligible. Equation 1 can be rearranged to solve for C_H , the component obtained during hillslope erosion in the source area, as:

$$C_H = (C_M - C_{Ex}) \cdot e^{-\lambda t} - C_B \quad (2)$$

For sediments excavated from depth z_s beneath the top of the outcrop surface, C_{Ex} can be calculated according to Val et al. (2016):

$$C_{Ex} = \sum_{i,j,k} \frac{P_{i,j,k}^{outcrop}}{\lambda + \frac{\rho_s \cdot \varepsilon}{\Lambda_{i,j,k}}} \left[e^{-\left(\frac{\rho_s \cdot z_s}{\Lambda_{i,j,k}} \right)} \right] \quad (3)$$

where $P_{i,j,k}^{outcrop}$ is the surface production rate ($\text{atoms g}^{-1} \text{yr}^{-1}$) of ^{10}Be by neutron spallation and fast and stopped muon reactions at the sampling locations, ρ_s is the density of the sampled sandstones (g cm^{-3}), ε is the exhumation rate (cm yr^{-1}), and $\Lambda_{i,j,k}$ is the effective attenuation length (g cm^{-2}) of neutrons and fast and stopped muons. For sediment subject to an accumulation rate (cm yr^{-1}), A_c , the concentration acquired during burial, C_B , can be estimated as (Braucher et al., 2000; Charreau et al., 2011):

$$C_B = \sum_{i,j,k} \frac{P_{i,j,k}^{basin}}{\lambda - \frac{\rho_s \cdot A_c}{\Lambda_{i,j,k}}} \left[e^{-\left(\frac{\rho_s \cdot A_c}{\Lambda_{i,j,k}} \right)} - e^{-(\lambda t)} \right] \quad (4)$$

Table 1

Parameters Used in the Paleoerosion Rate Calculations (Equations 2–5), With Their Values, Uncertainties, and References

(A) Parameter	Symbol and unit	Value	1σ	References
^{10}Be decay constant	λ (yr $^{-1}$)	4.998×10^{-7}	0.043×10^{-7}	Chmeleff et al. (2010); Korschinek et al. (2010)
Sea-level high-latitude ^{10}Be production rate				
Neutrons	P_i (at g $^{-1}$ yr $^{-1}$)	4.09	0.35	Phillips et al. (2016)
Fast muons	P_j (at g $^{-1}$ yr $^{-1}$)	0.024	0.005	Braucher et al. (2003, 2011)
Stopped muons	P_k (at g $^{-1}$ yr $^{-1}$)	0.027	0.001	Braucher et al. (2003, 2011)
Attenuation length				
Neutrons	Λ_i (g cm $^{-2}$)	160	10	Lal (1991)
Fast muons	Λ_j (g cm $^{-2}$)	4,320	950	Braucher et al. (2003, 2011)
Stopped muons	Λ_k (g cm $^{-2}$)	1,510	100	Braucher et al. (2003, 2011)
Density				
Bedrock	ρ_r (g cm $^{-3}$)	2.7	0.5	Charreau et al. (2011); Puchol et al. (2016)
Sediment	ρ_s (g cm $^{-3}$)	2.5	0.1	Tamrakar et al. (1999); Charreau et al. (2011)
Basin-average				
(B) Scaling factors	Yamuna	Piedmont	Burial site	Sampling site
Neutrons	3.33	1.37	0.69	1.16
Muons	2.64	1.13	0.95	0.99

where $P_{i,j,k}^{\text{basin}}$ is the ^{10}Be surface-production rate by neutron spallation and fast and stopped muon reactions at the depositional site, and ρ_s is the density of the overlying sediment. After obtaining paleo- ^{10}Be concentrations (C_H) by solving Equations 2–4, the catchment-average paleo-erosion rate, ϵ_p , can be derived using the equation (Lal, 1991):

$$\epsilon_p = \sum_{i,j,k} \frac{\Lambda_{i,j,k}}{\rho_r} \left(\frac{P_{i,j,k}^{\text{source}}}{C_H} - \lambda \right) \quad (5)$$

where $P_{i,j,k}^{\text{source}}$ is the catchment-average production rate of ^{10}Be by neutron spallation and fast and stopped muons and ρ_r is the density of the source rock.

Uncertainties for the reconstructed paleo- ^{10}Be concentrations (C_H) and erosion rates were derived using a Monte Carlo approach following Val and Hoke (2016). As the values of parameters in Equations 2–4 can not be negative and can vary over several orders of magnitude, we assumed that they form a log-normal distribution (Limpert et al., 2001) from which we drew random populations using the parameters' mean and standard deviation. Each parameter forms a vector of 10,000 random values. These vectors were subsequently used to compute 10,000 different random outputs of Equations 2–4. At the end of the computation, the paleo- ^{10}Be concentration (C_H) and uncertainty values for each sample were obtained from the mean and two standard deviations of the 10,000 random outputs of Equation 2. Finally, the $C_H \pm 2\sigma$ values were used to estimate the paleo-erosion rate and its uncertainties. Variables and constraints on the parameters in Equations 2–5 are provided in Table 1.

3.4.1. Constraints on the History of Sediment Accumulation and Burial for Determining C_B

One of the difficulties in accurately reconstructing the paleo- ^{10}Be concentrations (C_H) is the uncertainty on the sediment burial rates and, thus, on the estimation of C_B . Previous analysis of ^{10}Be in older foreland basin sediment of the Tianshan range (Central Asia) and Andes suggest that C_B can account for up to 35%–40%

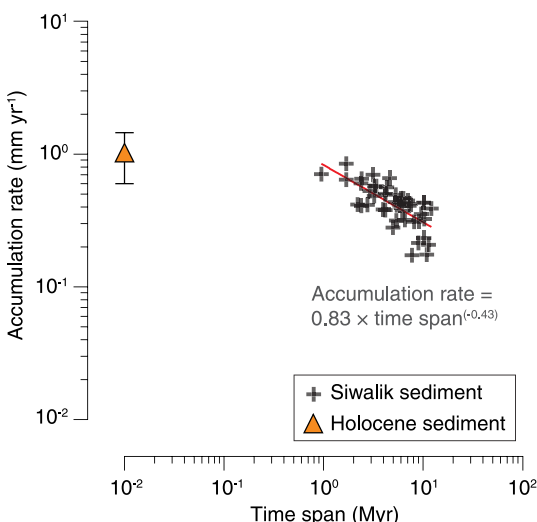


Figure 6. Sediment accumulation rates for the past ~12 Myr in the Himalayan foreland basin as a function of geological time. Values are plotted on a log-log scale to make the Sadler effect evident. Rates were estimated using the published magnetostratigraphy of the Siwalik sections. Thick red line = power-law fit to the data.

of C_M (Charreau et al., 2011; Madella et al., 2018; Puchol et al., 2016; Val et al., 2016). Although magnetostratigraphy provides constraints on the long-term rate of sediment accumulation (Charreau et al., 2011; Madella et al., 2018; Oskin et al., 2017; Puchol et al., 2016), this rate does not provide a reliable measure of the burial rate to a depth of a couple of meters, where the production of cosmogenic nuclides is close to zero. The reason for this is the so-called “Sadler effect” (Sadler, 1981), which describes that sediment accumulation rate decreases as a power-law function of the interval of time over which it is measured. This apparent decrease in accumulation rate arises because of incorporation of longer hiatuses in deposition as averaging time is increased. Indeed, our compilation of sediment accumulation rates in the late Cenozoic Himalayan foreland basin, estimated using the published magnetostratigraphy of 44 sections and averaged over ~1–12 Myr, indicates that accumulation rates decrease systematically with measurement duration (Figure 6). As shown later (Section 4), magnetostratigraphy-derived long-term sedimentation rate would yield too high C_B values for some samples, implying that this long-term rate is too low, which agrees with our compiled data. In the absence of any other means for deriving each samples’ actual burial rate (i.e., the rate averaged over the time taken to bury grains as a sedimentary deposit beyond the penetration depth of cosmic rays), we used a range of Holocene burial rates ($0.06\text{--}0.145\text{ cm yr}^{-1}$) in the proximal Himalayan foreland basin, averaged over a time period of 700–2,500 years, that was calculated using radiocarbon ages of organic material by Sinha et al. (1996).

Furthermore, we computed accumulation rates from all pairs of dated paleomagnetic events in our study section, and plotted them against time span and contoured for net thickness (Figure S4), following the approach of Sadler and Jerolmack (2014). An average regression line extrapolated back to a critical burial depth of ~2 m (i.e., the depth where production rates are <10% of surface production) predicted an accumulation/burial rate, which is consistent with the one that we used for the estimation of C_B .

The wet bulk density of the overlying sediment (ρ_s) was assumed to be equal to $2.5 \pm 0.1\text{ g cm}^{-3}$, based on measured densities for Siwalik sandstones from western Nepal (Tamrakar et al., 1999). A similar density value was also used in previous studies to reconstruct C_B from older foreland basin sediment (e.g., Charreau et al., 2011; Madella et al., 2018; Puchol et al., 2016). The location of the depositional site, which is relevant for scaling the ^{10}Be production rate during sediment burial, was assumed to be at the elevation of the modern Gangetic plain ($300 \pm 50\text{ m}$ above sea level), at a latitude of 30.2°N . Previous analysis of pedogenic carbonates from the same section yielded $\delta^{18}\text{O}_{\text{sc}}$ values that support sediment deposition at low (<400 m) elevation (Sanyal et al., 2004).

3.4.2. Constraints on Uplift and Erosion of the Siwalik Units to Determine C_{Ex}

The >100 m thick conglomerates that are lying above our youngest samples suggest that all samples were buried sufficiently to depths completely shielded from cosmic radiation. The exhumation of the Siwalik units due to uplift of the Dhanaura anticline began post-0.60 Ma (Barnes et al., 2011). Our sampling sites were located 2.4–15 m beneath the present-day outcrop surface, which is insufficient to shield all samples entirely from the recent (i.e., post-0.60 Ma) exposure to cosmic rays. Recent exhumation rates of the Siwalik rocks that are exposed along the core of the Dhanaura anticline are unconstrained but can be estimated using the empirical relationship between normalized channel steepness (k_{sn}) and rock uplift rate that has been calibrated to Siwalik rocks in central Nepal (Kirby & Whipple, 2012). This approach has been shown to yield reasonable results for the nearby Mohand anticline (Kirby & Whipple, 2012), which is the eastward continuation of the Dhanaura anticline, ~50 km to the southeast of our study area (Figure 2a). Our analysis of channel profiles of 14 streams developed across the southern flank of the Dhanaura anticline exhibit a mean k_{sn} of 14.1 ± 3.5 , which predicts an average uplift rate of $3 \pm 1\text{ mm yr}^{-1}$ that we use as an exhumation rate estimate for the Dhanaura anticline (Figure S5).

3.4.3. ^{10}Be Production Rate

In order to determine paleo-erosion rate, the production rate of ^{10}Be in the sediment source area ($P_{i,j,k}^{\text{source}}$ in Equation 5) must be known. Although the precise paleo-production rates of cosmogenic ^{10}Be in sediment source areas are unknown, the present-day production rates can be considered approximations of the actual values (e.g., Charreau et al., 2011; Lenard et al., 2020; Oskin et al., 2017; Puchol et al., 2016; Val et al., 2016). We therefore used the modern catchment-average ^{10}Be production rate of the Yamuna ($\sim 14 \text{ atoms g}^{-1} \text{ yr}^{-1}$ for production by spallation) and the piedmont catchments ($\sim 6 \text{ atoms g}^{-1} \text{ yr}^{-1}$, an average of 16 catchments that drain the hanging wall of the Paonta Thrust) for calculating paleoerosion rates. The source catchments were inferred based on the sediment provenance data (see Section 2.3). We scaled the sea-level high-latitude ^{10}Be production rates of neutrons, fast muons, and stopped muons, respectively (Table 1), using the Lifton-Sato-Dunai nuclide-independent scaling scheme (Lifton et al., 2014).

3.4.4. ^{10}Be -Derived Modern Erosion Rates and Sediment Fluxes

Measured ^{10}Be concentrations of modern sediment samples were converted to catchment-average erosion rates using Equation 5. The effective elevations (i.e., the production-rate weighted average elevation) and effective latitudes for individual basins were calculated to determine the elevation/latitude scaling factors of neutrons, fast muons, and stopped muons, respectively, using the CRONUS Earth Web Calculators version 2.1 (<http://cronus.cosmogenicnuclides.rocks/2.1/>). The catchment-average ^{10}Be production rates of neutrons, fast muons, and stopped muons were calculated by scaling the sea-level high-latitude reference ^{10}Be production rate (Table 1). Modern sediment fluxes (Q_s) of the Yamuna River and its tributaries near the mountain front (Figure 1c) were estimated from the ^{10}Be -derived erosion rates using the equation, $Q_s = \varepsilon \cdot \rho_r \cdot A$, where ε is the erosion rate, ρ_r is the density of the eroded material (2.7 g cm^{-3}), and A is the catchment surface area.

4. Results

The ^{10}Be concentration in modern Yamuna sediment (sample# Ya17-01) is $(15.87 \pm 0.98 [1\sigma]) \times 10^3 \text{ atoms g}^{-1}$. The ^{10}Be concentration in modern piedmont sediments (samples# SM18-01, SM18-02, and SM18-03) range from 3.47×10^3 to $6.70 \times 10^3 \text{ atoms g}^{-1}$ (Figure 7a). The measured ^{10}Be concentrations in paleo-Yamuna sediments range from 0.91×10^3 to $7.06 \times 10^3 \text{ atoms g}^{-1}$, with relative uncertainties of 7%–13%, whereas the measured ^{10}Be concentrations in paleo-piedmont sediments range between 0.85×10^3 and $2.19 \times 10^3 \text{ atoms g}^{-1}$, with relative uncertainties of 10%–15% (Figure 7b). All measured ^{10}Be concentrations of our paleo-samples are in agreement with the radioactive decay of modern concentrations of the Yamuna and piedmont samples, respectively (Figure 7b).

The reconstructed concentrations of ^{10}Be in paleo-sediments prior to their burial in the foreland basin (i.e., C_H) average to $(10 \pm 15 [2\sigma]) \times 10^3 \text{ atoms g}^{-1}$ over the past ~ 6 Myr, with variations between $(0.4 \pm 1.6 [2\sigma]) \times 10^3$ and $(36.9 \pm 6.8) \times 10^3 \text{ atoms g}^{-1}$. Furthermore, the paleo- ^{10}Be concentrations have two distinct probability peaks (Figures 7c and 7d). A low concentration ($< 5 \times 10^3 \text{ atoms g}^{-1}$) peak covers those samples that we identified as paleo-piedmont sediment. A high concentration ($> 5 \times 10^3 \text{ atoms g}^{-1}$) peak corresponds largely to those sediment that we consider to be deposited by the Yamuna River. The C_H in paleo-Yamuna sediments show larger variability, by a factor of six (Figure 7e). The fraction β —calculated as $[(C_B + C_{Ex})/C_H \cdot e^{-(\lambda \cdot t)}]$ —has been proposed as a metric for assessing the proportion of the C_M that is made of post-depositional dose, and β values as high as ~ 1 have been reported as an acceptable maximum (Schaller & Ehlers, 2006; Schaller et al., 2004). β ratios for paleo-Yamuna samples are consistently < 0.4 , whereas paleo-piedmont samples yield β ratios ~ 1 except for three samples, which have β value > 2 . In the latter cases ($\beta > 2$), the 2σ uncertainty of the final C_H concentration is greater than the mean; therefore, only a minimum paleo-erosion rate (Figure 8a) was estimated from the concentration $C_H + 2\sigma$.

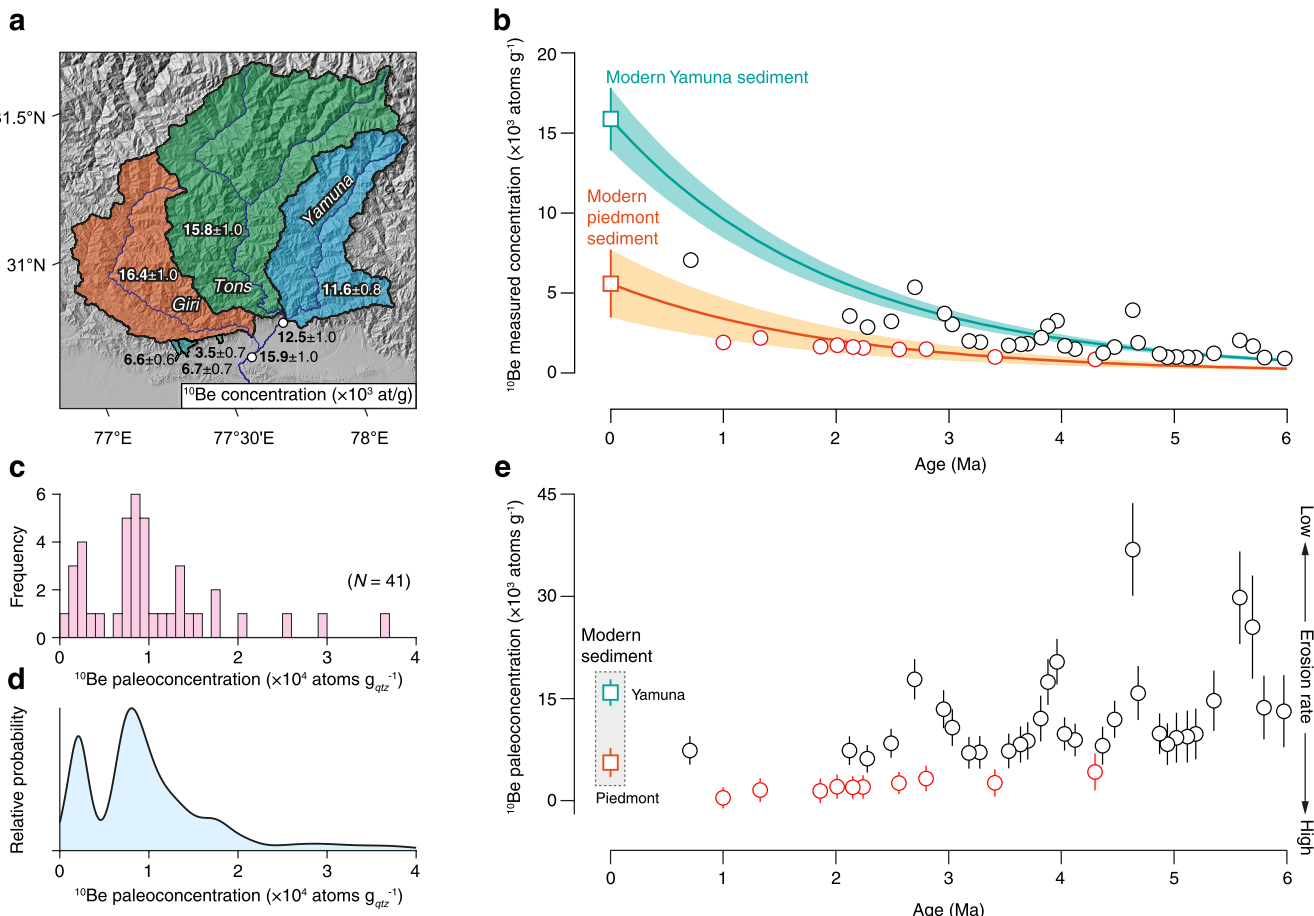


Figure 7. Cosmogenic ^{10}Be record. (a) Map of the Yamuna catchment and ^{10}Be concentrations of analyzed modern river sediments. Colored surfaces indicate the major hydrological basins upstream of the sampling locations. White circles indicate the sampling locations along the Yamuna trunk stream, between the Main Boundary Thrust and Main Frontal Thrust. (b) Measured ^{10}Be concentration in the modern and paleo-sediments, respectively. The empty orange rectangle and the error bar corresponds to the mean $\pm 2\sigma$ of the ^{10}Be concentrations measured in three piedmont samples (SM18-01 to SM18-03). Solid color line and shaded envelope (2σ uncertainty) show the predicted concentration after radioactive decay of modern measurements. Empty black circles = paleo-Yamuna sediment; empty red circles = paleo-piedmont sediment (see Section 2.3). Note that the modern Yamuna sediment at our sampled location integrates the flux from the Yamuna, Tons, and Giri catchments in (a). (c and d) Histogram and probability density plot of reconstructed paleo- ^{10}Be concentration. (e) Reconstructed ^{10}Be concentrations in paleo-Yamuna and paleo-piedmont sediments prior to the burial in the foreland basin. Error bars represent 2σ uncertainty derived from 10,000 random variations of input parameters for each sample (see Section 3.4).

The reconstructed paleo-erosion rates of the piedmont catchments range between $1.2_{-0.4}^{+1.7}$ (2σ) and $2.0_{-0.9}^{+7.0}$ mm yr^{-1} , and reflect, within error, the present-day value ($0.8_{-0.6}^{+0.6}$ mm yr^{-1}). The dispersion in paleo-piedmont erosion rates is smaller than for the paleo-Yamuna erosion rates (Figures 8a and 8b). The modern erosion rate of the Yamuna catchment is $0.7_{-0.2}^{+0.2}$ mm yr^{-1} . Paleo-erosion rates of the Yamuna catchment range between $0.3_{-0.04}^{+0.1}$ and $1.6_{-0.4}^{+0.8}$ mm yr^{-1} and appear to exhibit a quasi-cyclic pattern (Figure 8b). Spectral analysis (see Text S1) of the erosion rate record reveals that an ~ 1 -Myr-long periodicity is the most probable (Figures 8b and S6). However, these “cycles” are not of equal duration, and shorter periods can be observed. In general, we observe low-erosion-rate troughs that are defined by 3–4 samples that each span ~ 200 –500 kyr, whereas the intervening peaks are broader, defined by 3–5 samples, and somewhat longer, spanning ~ 500 –800 kyr. We additionally tested the sensitivity of the paleo-erosion rate cyclicity with respect to two end-member burial scenarios: one that assumes immediate deep burial beyond the cosmic ray penetration depth (Figure S7) and another one, in which we assumed that burial occurs at a rate equal to the long-term average sediment accumulation rate (0.5 ± 0.1 mm yr^{-1}) over the entire section, determined from magnetostratigraphy (Figure S8). In the latter scenario, the paleo- ^{10}Be concentrations (C_H) of 10 samples

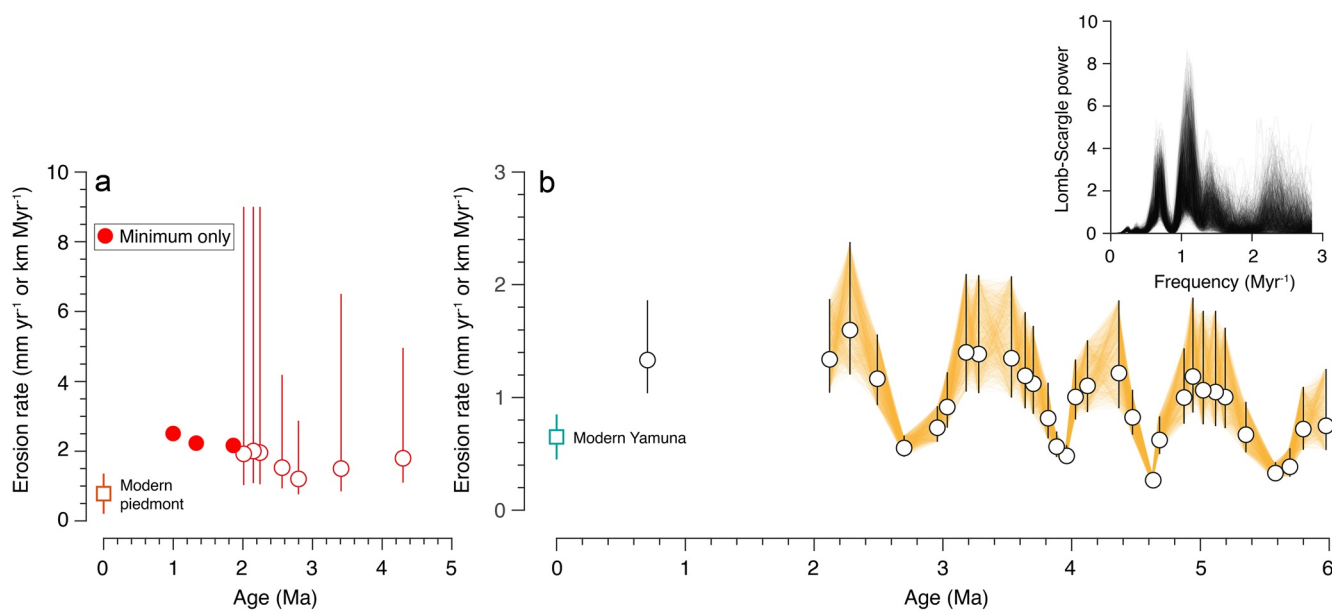


Figure 8. Reconstructed erosion rates as a function of the timing of sediment depositional age. (a) Modern and paleo-erosion rates of the piedmont catchments, calculated from reconstructed paleo-¹⁰Be concentrations in case of paleo-sediments. (b) Modern and paleo-erosion rates of the Yamuna catchment, calculated from reconstructed paleo-¹⁰Be concentrations in case of paleo-sediments. The ¹⁰Be integration time of individual samples is 0.24 ± 0.04 to 2.26 ± 0.60 kyr. The orange lines in the background connect the 10,000 possible erosion rates predicted by the Monte Carlo approach. Inset shows the Lomb-Scargle periodogram (see Text S1) computed from the erosion rate data.

yielded negative values, suggesting a too low accumulation rate and thus too high C_B . Nevertheless, results show that independent from the burial scenario, the periodicity reported in Figure 8b remains unaltered. Although we acknowledge that the pattern we observe is not strictly cyclic, as periods appear to change somewhat, we will refer to them as cyclic from now on for brevity. Finally, in addition to the cyclic pattern, it appears that the mean erosion rate increased toward the present (Figure 8b).

5. Discussion

5.1. Climatic Versus Tectonic Origin of Cyclic Erosion Rates

Intermittency in foreland basin sediment deposition could potentially lead to cyclic variations in ¹⁰Be production during burial. This may be a factor in our study section, where the depositional record documents the imprint of channel avulsion (Sections 2.2 and 2.3). If we assume a steady input signal (paleoerosion rate) from the Himalayan hinterland and consider a ¹⁰Be surface production rate of ~ 3 atoms g⁻¹ yr⁻¹ (based on modern production rate) at the foreland, the $\sim 15,000$ atoms g⁻¹ differences in ¹⁰Be paleoconcentration that we observe within a cycle (Figure 7e), would require ~ 5 kyr of continuous near-surface exposure. Given that the decrease in cosmogenic-nuclide production below the surface is approximately exponential with a half-mass depth of about 100 g cm⁻² (Lal, 1991), sediment residence at a depth of ~ 1 m below the surface would require around 25 kyr of continuous exposure. However, studies from the fan areas of proximal Himalayan foreland basin suggest quite rapid and frequent avulsions. For example, the contemporary Kosi River in the eastern Gangetic plain has recorded a total migration of about 110 km in the last 200 years (e.g., Wells & Dorr, 1987). We thus deem it highly unlikely that the observed cyclicity could be attributed to the internal river-dynamics-related intermittency in sediment accumulation. In addition to the unlikely prolonged exposure, we found no indication for a systematic ~ 1 -Myr cyclicity in burial that could be confidently linked to the observed pattern. Therefore, we suggest that the observed pattern is related to erosion in the source area, and not to burial in the foreland basin.

The observed quasi-cyclic variations in erosion rates over the past 6 Myr implies that the forcing leading to such variations is presumably cyclic, too. Cyclic forcings may occur due to variations in the Earth's orbital

parameters, causing, for example, the so-called Milankovitch cycles that resulted in the late Cenozoic periodic glaciations (e.g., Zachos, 2001) and variations in the intensity of monsoonal precipitation (e.g., Y. Wang et al., 2008). We argue below that the tectonic growth of the Himalaya by punctuated crustal accretion can also exert a cyclic forcing, thus providing an alternative explanation for the observed Myr-long periodicity in erosion rates.

Previous studies have shown evidence of enhanced erosion during periods of extended ice cover in many high-latitude or high-elevation mountain belts worldwide (e.g., Herman et al., 2013; Valla et al., 2011). This link of erosion and climate has been attributed to the orbitally controlled late Cenozoic onset of periodic glaciations (e.g., Zachos, 2001). However, the periodic variation in erosion rates reported in our study appears to predate the onset of large amplitude glacial cycles at ~1 Ma (Zachos, 2001) and thus cannot be attributed to this driver. The long-period astronomical cycles (Milankovitch “grand cycles”) associated with the amplitude modulation of Earth’s axial obliquity cycle (~1.2 Myr) and climatic precession cycle (~2.4 Myr) (Crampton et al., 2018) have also been suggested as controls on late Cenozoic ice sheet history (Pälike et al., 2006). Even if these grand cycles would have modulated climate, they are unlikely to affect the erosional response of the rapidly uplifting Himalaya. For such long climatic forcing periods, the landscape is able to change its shape (steepness) and thus adjust to the slow variations in climate. As a result, erosion rates would remain almost equal to the tectonic uplift rate (Braun et al., 2015). These grand cycles are thus unlikely to be recorded in the foreland basin sedimentary record.

Similarly, the variability in monsoonal rainfall intensity has been invoked to control the temporal change in Himalayan erosion (Bookhagen et al., 2005; Clift et al., 2008); but the empirical data (e.g., Gourlan et al., 2010; Y. Wang et al., 2008), as well as estimates from global circulation models (Braconnot, 2004), suggest that monsoonal rainfall intensity varies in phase with temperature at orbital cycle periods, with major periodicities at 23, 41, 100, and 400 kyr. Therefore, they are unable to explain the Myr-long periodicity. The $\delta^{18}\text{O}$ (a proxy to changing climate) and ε_{Nd} (a proxy for the intensity of sedimentary input from Himalayan rivers) values of the Bengal Fan sediments suggest that climate-driven changes in the erosional flux from the Himalaya are likely to be recorded in sedimentary archives close to the sediment source areas (Gourlan et al., 2010). However, the temporal resolution of our samples does not allow us to resolve such high-frequency climate-driven changes in erosion rate. Even if we assume that higher-frequency variations are present throughout the 6-Myr interval, the presence of ~1-Myr periodicity suggests that shorter-period variations are of lower magnitude and thus not obscuring the longer-term signal.

Alternatively, we suggest that the observed periodic variation in erosion rates could be a consequence of the tectonic growth of the Himalaya. Orogenic wedges, like the Himalaya, grow primarily by frontal and basal accretion of crustal rocks, which each lead to distinct rock uplift patterns (e.g., Gutscher et al., 1996; Menant et al., 2020; Mercier et al., 2017; Naylor & Sinclair, 2007; Zilio et al., 2020). Although, the geological record of the Yamuna catchment documents late Cenozoic orogenic growth by both frontal and basal accretion (see Section 2.1), frontal accretion as a driving mechanism to explain the observed cyclicity is unlikely. Based on our measured ^{10}Be concentrations in modern river sediment, we estimated that ~14% of the sediment flux of the Yamuna River near the mountain front is delivered from the Giri catchment, which is the southernmost tributary of the Yamuna River and which drains the region of frontal accretion (Figure 1c). To account for the observed cyclicity, erosion rates in the Giri catchment would have to vary by at least ~110% (based on sediment flux estimates derived from modern erosion rates and catchment areas), relative to modern rates, which is unlikely, specifically in light of the limited areal extent of frontally accreted units in this catchment (Figure 1c, ~9% of the Giri catchment and ~2% of the entire Yamuna catchment). Furthermore, over the last ~4.5 Myr, the relatively steady erosion rate of the piedmont catchments—developed in the foreland fold-and-thrust belt—argues against frontal accretion as a driver of erosional cyclicity in the Himalaya.

The region affected by basal accretion through the development of a duplex at depth, on the other hand, is entirely contained in the upper Yamuna catchment, which exports sediment analogous to the composition of our analyzed sandstone samples. Moreover, the spatially averaged erosion rates would have to vary by no more than ~60%, relative to modern erosion rates, to explain the observed cyclicity. In addition, the timescale of basal accretion is consistent with the observed cyclicity in erosion rates. The typical lengths of basal-accreted thrust sheets that we estimated using restored balanced structural cross sections across the Himalaya in the vicinity of our study area (S. Mandal et al., 2019; Srivastava & Mitra, 1994; Webb, 2013),

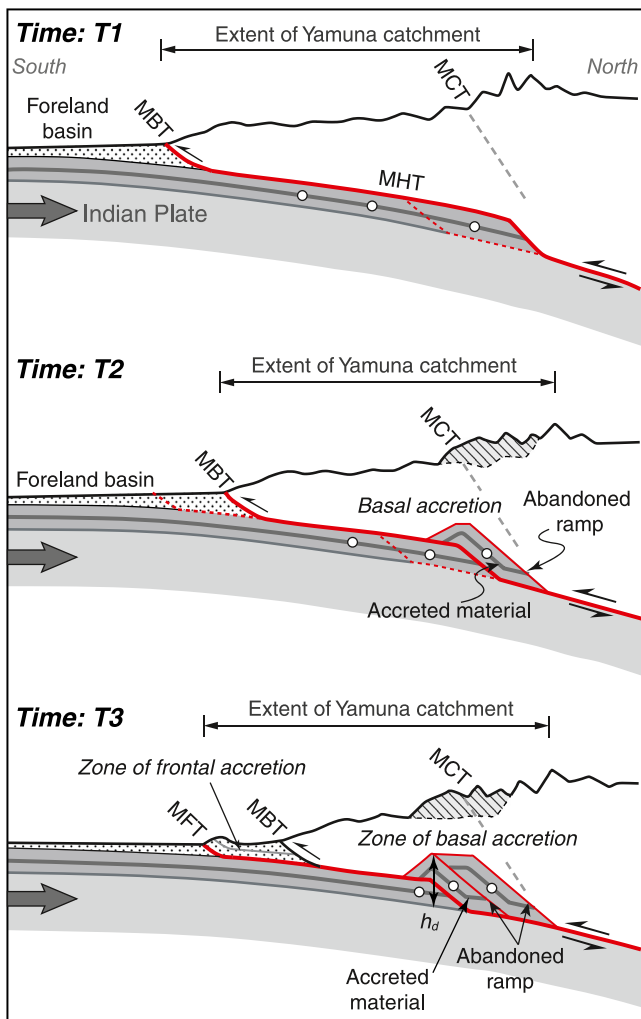


Figure 9. Schematic portrayal of basal accretion by duplex formation and resulting mountain building in the Himalaya. Thick red line indicates active thrust fault with the punctuated southward migration of steeper ramp segment—in contrast to one that is much larger and shallowly dipping—along the Main Himalayan Thrust (MHT), which leads to transfer of material from the underthrusting Indian plate to the orogenic wedge (i.e., the basal accretion between T_1 and T_2). As the steeper ramp propagates southward, more thrust sheets (abandoned ramps; thin red line) are incorporated into the orogenic wedge. Hatched region indicates the topography created in response to the basal accretion. Dashed red line indicates the future location of the steeper ramp segment and the length of the crustal unit that will be transferred from the Indian plate to the Himalayan wedge by basal accretion at stages T_2 and T_3 . Note that the thickness of the accreted thrust sheets (i.e., the height of the duplex, h_d) controls the vertical growth, whereas frontal accretion (T_3) controls the lateral growth of the thrust wedge, respectively. Note the low-relief topography at the toe of the thrust wedge that has been created in response to frontal accretion.

erosion rates would first be higher than uplift rates because the landscape is still adjusted to a higher uplift rate, followed by a gradual decrease in erosion rates as a new topographic steady state is approached.

range between 14 and 40 km (Figure S9). These displacement lengths of the accreted thrust sheets, when divided by a mean underthrusting velocity of the Indian plate beneath the Himalaya of $\sim 12 \text{ mm yr}^{-1}$ (Avouac, 2015), yield a maximum $\sim 1\text{--}3$ -Myr-long periodicity of basal accretion events (Naylor & Sinclair, 2007). This is consistent with our observation. This range of values is further consistent with the outcome of numerical experiments by Zilio et al. (2020), in which they considered an intermediate décollement with frictional strength lower than the basal décollement, constrained by the topography of the Himalayan wedge. We emphasize, however, that the duration of basal accretion cycles likely varies with time and does not follow a perfectly regular pattern. This expectation is based on the most likely non-uniform thickness of the thrust sheets that are basally accreted to the orogenic wedge and the observation that the thrust sheets' thickness determines their length and the timescale of the tectonic cycle (Naylor & Sinclair, 2007).

5.2. Plausible Impact of Basal Accretion on Erosion Rates

Basal accretion by duplex formation provides a mechanism of internal deformation and associated changes in topography (e.g., Adams et al., 2016; Menant et al., 2020; Mercier et al., 2017). According to this process, the flat-ramp-flat geometry of the MHT is expected to cause rock uplift above the ramp. Over longer time scales, abandonment of an old and the formation of a new ramp along the MHT due to episodic brittle failure within the Indian plate (Bollinger et al., 2006; Herman et al., 2010; Mercier et al., 2017; Zilio et al., 2020) induces a transient topographic adjustment to the new tectonic uplift pattern (Figure 9). Such topographic adjustments to basal accretion are presumably ongoing in western Nepal (Harvey et al., 2015) and in the Bhutan Himalaya (Adams et al., 2016), where low-relief landscapes with low-erosion rates exist at $\sim 3\text{--}4$ km elevation above sea level. In the Bhutan Himalaya, these landscapes are interpreted to have been formed *in situ* as they were uplifted ~ 1 km in the past $\sim 0.8\text{--}1$ Ma by the formation of structural duplexes at depth (Adams et al., 2016).

The ^{10}Be concentration of sediments eroded from the upland catchments could respond to the newly created transient topography in two ways. First, topographic growth above the new ramp would inevitably entail a change in the altitudinal distribution of catchment surface area (i.e., hypsometry) and, thus, the production rate of ^{10}Be (herein referred to as “production-rate-change effect”), which increases with altitude (Lal, 1991). The surface uplift would thus be accompanied by an increase in the ^{10}Be production rate, which in turn would lead to an increase of ^{10}Be concentrations in sediments exported to the foreland basin, yielding an apparent decrease in erosion rates, even if actual erosion rates would remain relatively invariant. Second, the focused uplift above the ramp will also lead to changes in erosion rate (herein referred to as “erosion-rate-change effect”). During phases in which topography grows, erosion rates would be slower than uplift rates because the landscape is not adjusted yet to the new uplift pattern. However, when a ramp is abandoned,

In summary, the tectonic growth of the Himalaya by punctuated basal accretion provides a plausible explanation why ^{10}Be -derived paleo-erosion rates exhibit a quasi-cyclic pattern with a ~ 1 -Myr-long period that arises from actual and apparent changes in erosion rate. However, without knowing how the topography looked like in detail in the past, it is difficult to quantitatively disentangle the “production-rate-change effect” from the “erosion-rate-change effect” on measured ^{10}Be concentrations in ancient foreland basin sediments. To further test if our hypothesis is physically plausible and what the potential magnitudes of these two effects could be, we used a numerical landscape evolution model.

5.2.1. Landscape Evolution Modeling

To demonstrate that episodic basal accretion can affect temporal erosion rates, we performed numerical landscape evolution simulations with the TopoToolbox Landscape Evolution Model (see details in Appendix A) (Campforts et al., 2017; Schwanghart & Scherler, 2014). A complex tectonic model of basal accretion is beyond the scope of this discussion. Instead, we simulated the spatial and temporal pattern in rock uplift that would result from episodic basal accretion by duplex formation at depth, similar to a previous study by Adams et al. (2016), in which the authors have explored the influence of an active duplex on the topography of the Bhutan Himalaya. To simulate how basal accretion affects landscapes repeatedly over several million years of plate convergence, we moved the high rock-uplift zone across the model domain for 2 Myr, consistent with the ramp formation-advection cycle that has been proposed earlier for the Himalaya (Mercier et al., 2017). We tested a range of parameter values (e.g., the high uplift zone’s width, rate of migration, uplift rates above the ramp and away from it) in accordance with observations from the Himalaya. In the following, however, we only refer to a simulation with parameter values as described in Appendix A. The results of our simulations are heuristic and illustrative to test how spatially varying rock uplift rates affect both actual and apparent variations in ^{10}Be -derived erosion rates.

The response of our experimental landscape to the migration of a crustal ramp toward the inner part of the system is shown in Figures 10a–10c. Soon after the onset of basal accretion, enhanced rock uplift rate over the ramp generates transient incision waves due to the formation of convex knickpoints in the longitudinal profile of channels that cross the region of basal accretion. As knickpoints migrate upstream, they move vertically because of the continued surface uplift created by the disequilibrium of rock uplift rates and erosion rates. The surface uplift subsequently steepens the river profiles below the knickpoint, which leads to a gradual increase in erosion rates of the adjacent hillslopes that lag with respect to the tectonic perturbation (Figure 10c). During the time period when the older ramp is abandoned, and a newer ramp is formed closer to the mountain front, accelerated erosion driven by fluvial downcutting continues to lower the surface topography over the older ramp at the backside of the newer ramp, leading to the topographic steady-state (characterized by equilibrium channel profiles). However, as the new ramp migrates toward the inner part of the range, tectonic rock uplift rate again outpaced the prevailing erosion rate, leading to vertical movement of knickpoints similar to the previous episode of basal accretion (Figure 10c). These feedbacks among the basal-accretion-driven rock uplift, river steepening, and erosion rate explain the cyclic temporal variability in topography and hence the commensurate variance in erosion rates.

When the ^{10}Be -derived erosion rate is calculated using the production rate in accordance with the topography of a specific time step, we precisely get the values of actual erosion rates. However, when we assume a constant production rate for the entire simulation period, as we do in our study, the two estimates disagree, leading to an increase in the amplitude of ^{10}Be -derived cyclic erosion rate variability (Figure 10d). This result implies that the surface-uplift-induced production rate effect would only change the amplitude of the cyclic variations—it would not change the cycles’ frequency or existence. Because the production rate effect is mostly related to variations in the height of the uplifted low-relief portion in the headwaters of the rivers that cross the high-uplift zone, any model parameters that affect this height also affect the amplitude of the apparent variations in erosion rate. For example, higher low-relief surfaces result from increasing uplift rates within the high-uplift zone, increasing its width, or reducing the erosional efficiency of river incision. All these modifications affect the resulting topography, hence the actual versus assumed variation in production rates that are ultimately responsible for the discrepancies between actual and ^{10}Be -derived erosion rates. The impact of potential sediment deposition and buffering from the higher parts of the land-

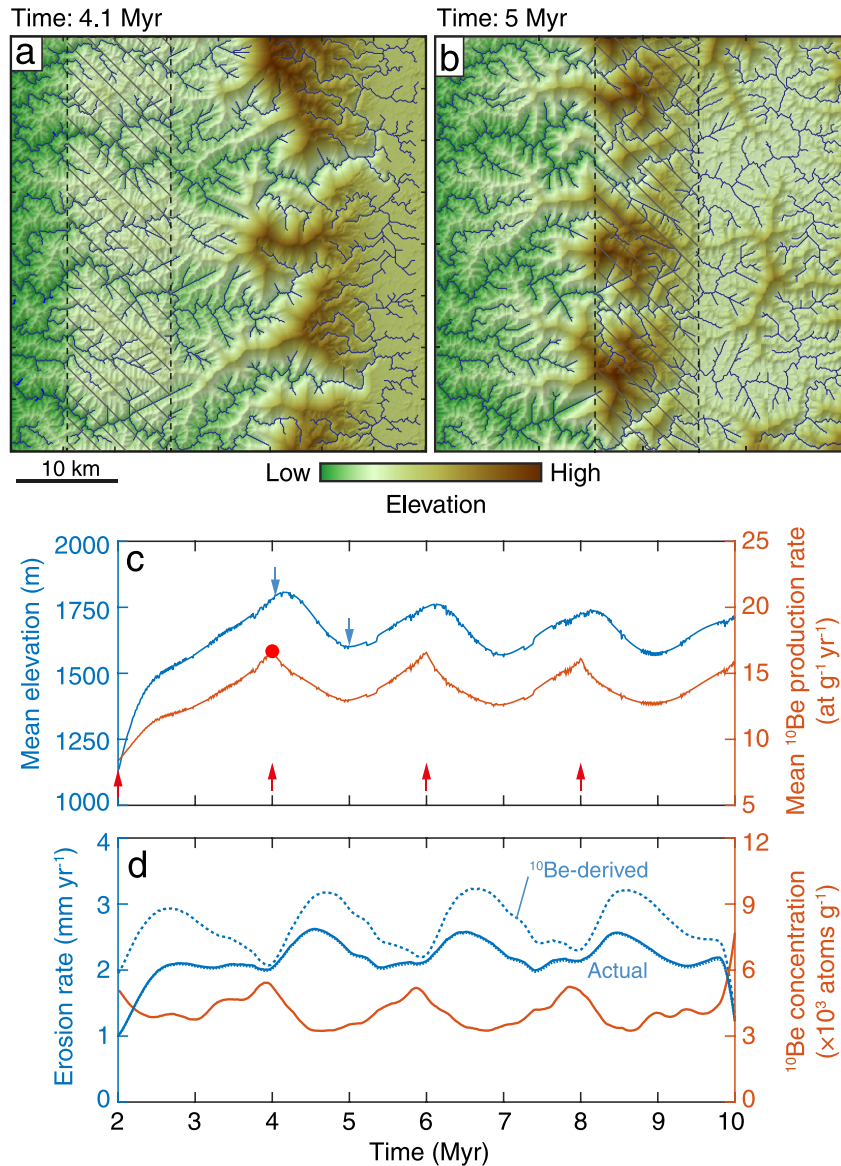


Figure 10. Evolution of topography, ^{10}Be production rate, and erosion rate through time after response to basal accretion by duplex formation at depth, simulated using the TopoToolbox Landscape Evolution Model. (a and b) Transient topographies after initial (a) and further response (b) to basal accretion, simulated by moving a 10-km-wide high rock-uplift zone across the model domain. The 10-km-wide hatched region experiences an uplift rate of 5 mm yr^{-1} , whereas the model domain outside the hatched region experiences a constant rock uplift rate of 1 mm yr^{-1} . (c) Evolution of the simulated mountain topography and the consequent variation of cosmogenic ^{10}Be production rate through time. Blue arrows indicate times when both topographic snapshots (a and b) are created. Red arrows mark the onset of high rock-uplift zone migration. (d) Simulated actual and ^{10}Be -derived erosion rates through time (for details, see Appendix A).

scape behind the orographic barrier (e.g., Adams et al., 2016) and changes in erosional efficiency due to the orographic enhancement of precipitation are not captured in our simulated erosion rates. Nevertheless, our simple numerical experiment indicates that episodic basal accretion by duplexing and consequent growth of the topography provides a plausible mechanism for the ^{10}Be -derived quasi-cyclic paleo-erosion rate variability that we observe.

5.3. Climatic Versus Tectonic Origin of the Long-Term Increase in Erosion Rates

In addition to the cyclic pattern, our reconstructed paleo-erosion rates of the Yamuna catchment also suggest a long-term increase over the past 6 Myr. The amplification of climate variability and repeated glaciations have been invoked to explain the worldwide acceleration of mountain erosion during the late Cenozoic (Herman et al., 2013; Molnar, 2004). However, the resolution and biases of the approaches that support increased erosion rates in response to late Cenozoic climatic cooling are intensely debated (Schildgen et al., 2018; von Blanckenburg et al., 2015; Willenbring & von Blanckenburg, 2010; Willett et al., 2020). A different view on this debate, however, resulted from the analysis of marine meteoric ^{10}Be / ^9Be isotope records that, when interpreted as a proxy of continental weathering and assuming that physical erosion increases concurrently with chemical weathering, suggest constant global erosion rates over the last 12 Myr (Willenbring & von Blanckenburg, 2010). This view is consistent with several ^{10}Be records from around the world that indicate no systematic increase in erosion rates over the Quaternary (e.g., Lenard et al., 2020; Mariotti et al., 2021; Osokin et al., 2017; Puchol et al., 2016). A limited impact of climate on erosion rates during the last glacial period has also been reported for the upper Yamuna catchment, based on ^{10}Be analysis in late Pleistocene terrace deposits (Kapannusch et al., 2020). From a more general point of view, theoretical treatments suggest that in regions where high tectonic uplift and erosion rates prevail, episodic climate changes would only transiently reduce or increase erosion rates (Braun et al., 2015). Because of the generally high background erosion rates in the Himalaya, any transient adjustments in topography, and thus, erosion rates, are therefore likely to be short (<1 Myr) (Braun et al., 2015; Whipple, 2009).

A climatic shift to progressively wetter conditions is a potential driver that can lead to the gradual increase in erosion rate by altering the erosional efficiency, as suggested previously for the European Alps (Willett et al., 2006). However, the Pliocene global cooling argues against a wetter climate during this period, consistent with several climate-proxy records indicating a reduction in Asian monsoon rainfall in the Pliocene (e.g., H. Wang et al., 2019). Moreover, the progressive foreland-ward growth of the Himalayan orogenic wedge is inconsistent with the climate-driven increase in erosional efficiency. The rate of stratigraphic onlap of the Siwalik Group onto the pre-Cenozoic basement of the Himalayan foredeep over the last 15 Myr has been estimated between 15 and 20 mm yr $^{-1}$, which is comparable to the present-day convergence velocity. This suggests that the convergence rates between the Indian and Eurasian plates have been relatively steady over the past ~15 Myr (Lyon-Caen & Molnar, 1985; Mugnier & Huyghe, 2006), which is also consistent with the rates estimated from the plate reconstructions by Molnar and Stock (2009). According to the predictions of the critical taper model, a climate-driven increase in erosional efficiency without any concomitant changes in tectonic convergence rate would have ceased the outward tectonic growth of the Himalaya to restore its critical taper (Stolar et al., 2006). The incessant progradation of sedimentary facies into the foreland over the last 15 Myr does not support a shrinking wedge. Instead, it documents a foreland-ward-propagating deformation front driven by the thrusting of the Indian plate beneath the Himalayan wedge (Avouac, 2015; Lyon-Caen & Molnar, 1985). Moreover, because climate changes would most likely occur synchronously along the Himalaya, long-term climate-related changes in sediment flux and erosion rate should be preserved in marine records. However, existing stratigraphic records show an increase in erosion and sediment flux only during periods of strong monsoon (Bookhagen et al., 2005; Goodbred et al., 2000) but no long-term increase (Galy et al., 2010; Lenard et al., 2020). Hence, we deem it unlikely that the long-term increase in erosion rates of the Yamuna catchment could be attributed to climate change over time.

Instead, we suggest that the observed long-term increase in erosion rates could possibly be the consequence of the progressive crustal shortening of the Himalayan thrust wedge (Figure 9). The northern limit of the present-day Yamuna catchment is characterized by a sudden ~2 km increase in the topography at a distance of ~130 km from the mountain front that coincides with the highest erosion rates (Figure S10). This observed pattern of erosion is interpreted to be controlled by localized uplift due to thrusting over a ramp in the MHT (Scherler et al., 2014), possibly in association with basal accretion (Mercier et al., 2017). During the period of basal accretion in the last at least 10 Myr (Figure 3; Colleps et al., 2019; S. K. Mandal et al., 2018), the successive MHT ramps have propagated southward relative to the previously active deformation front, the MBT (Bollinger et al., 2006; Herman et al., 2010; Mercier et al., 2017; Zilio et al., 2020). This episodic ramp migration led to the progressive addition of accreted thrust sheets to the Lesser Himalayan duplex, thereby engendering a progressive shortening, hence thickening of the Himalayan thrust

wedges across the Yamuna catchment with time. This inference is based on geological evidence from the Garhwal Himalaya, which documents that a significant fraction of Lesser Himalayan shortening has been accommodated by the growth of duplex structures in the middle part of the Yamuna catchment (Figure 1c) (Srivastava & Mitra, 1994). The theory of critical tapers predicts that the thickening of wedges should either be compensated by expanding the wedge laterally toward its foreland or increasing the erosional fluxes to maintain a constant taper (e.g., Dahlen, 1990). Although this holds true for many orogens, it does not apply readily to the Himalayas because of its segmented wedge geometry that is controlled by accretionary cycles and/or mechanical stratigraphy (e.g., Zilio et al., 2020). In fact, both analog and numerical models have shown that in the presence of weak mechanical layering within the wedge, the critical topographic slope above the zone of basal accretion can develop independently up to its own limit (Konstantinovskaya & Malavieille, 2005; Zilio et al., 2020). This implies that the basal-accretion-induced thickening should be compensated by accelerating the erosion rates, possibly due to orographic enhancement of precipitation that facilitates to maintain the critical topographic slope of the inner wedge. Circumstantial evidence, such as the late Miocene to Pliocene widespread unroofing of Lesser Himalayan duplex (Colleps et al., 2019; S. K. Mandal et al., 2018), argues in favor of this scenario. The observed long-term increase in erosion rates, therefore, could be attributed to the progressive shortening of the Yamuna catchment. However, for this hypothesized mechanism to be viable to explain the long-term increase in erosion rates further requires that the drainage divide be pinned above the zone of basal accretion, and that the migration of successive ramps shortens the catchment itself with time. Past studies from around the Himalaya support this assertion (e.g., Bollinger et al., 2006; Herman et al., 2010; Robert et al., 2011), suggesting that the highest topography is always above the ramp and that most major Himalayan rivers do not cross the highest topography; and if they do so, they enter the rain shadow and consequently erosion rate are much lower (e.g., Gabet et al., 2008). The recent (post-0.6 Ma) propagation of the deformation front toward the foreland (by frontal accretion) and the formation of the MFT sheet (Figures 2 and 9), however, effectively elongated the Yamuna catchment, which should encompass a reduction of erosion rates in the long-term—if measured south of the active deformation front, as applicable to our study.

6. Synthesis

Our findings support the idea that temporal variability in erosion rate within the Himalaya, and probably other orogenic belts, can result purely from the punctuated nature of tectonic accretion. These processes are inherent to the way fold-and-thrust belts grow at continental collisional zones. Despite relatively steady rates of plate convergence, uplift rates within thrust wedges typically vary spatially and temporally, owing to the formation of discrete thrust faults that remain active for finite periods (e.g., Gutscher et al., 1996; Konstantinovskaya & Malavieille, 2005; Naylor & Sinclair, 2007; Zilio et al., 2020). Because landscapes need time to adjust to changes in rock uplift (Whipple & Meade, 2006), such tectonic perturbations ought to entail periodic changes in surface uplift and thus topography and erosion rates (e.g., Menant et al., 2020). The timescale of the resulting tectonic cycles is controlled by both the convergent motion of the involved continental plates and the spacing of the accreted thrust sheets (Naylor & Sinclair, 2007), and they superimpose on any potential climate-induced changes in erosion rate (Herman et al., 2013). In the mostly unglaciated Yamuna catchment, the tectonic cycles appear to dominate erosion rate changes during the late Cenozoic era. This may be true for other convergent orogens, where the tectonic cyclicity covers similar timescales (Naylor & Sinclair, 2007), although heavily glaciated orogens may be exceptions (e.g., Berger et al., 2008).

Furthermore, the above-pictured processes hold potential for feedbacks between the tectonic growth and erosional demise of the mountain topography. If basal accretion by duplex formation leads to topographic growth over ~2–3 km in elevation, for example, due to the thickness of the accreted thrust sheets and, therefore, the height of the duplex (Figure 9), the ensuing topography could enhance monsoonal rainfall and create a rain shadow, which could further change the pattern of erosion rates across the range (Sobel et al., 2003). For instance, in the Bhutan Himalaya, rainfall is high at the range front but much reduced over the elevated and slowly eroding low-relief landscape (Adams et al., 2016). Moreover, if frontal accretion is infrequent relative to basal accretion, as in the Garhwal Himalaya (Srivastava & Mitra, 1994), in that case, continuous crustal shortening increases the topography by the growth of the duplex in the internal part of the thrust wedge. Consequently, the erosion rate would have to increase in order to maintain a stable wedge

form. Such feedbacks could further influence the force balance on active faults and hence the distribution and propagation of deformation within orogenic wedges, and thus the pattern of erosion (Whipple, 2009).

Our study highlights that a sedimentary archive close to the source catchment holds the potential to preserve much of the tectonically related erosion rate variability of the hinterland. Unlike the orbital-scale changes in monsoon intensity that could co-occur across the entire Himalaya, tectonically driven cycles are likely to be asynchronous along the Himalaya (e.g., Mercier et al., 2017), and therefore unlikely to be preserved in sediments of the Bengal and Indus fans (e.g., Galy et al., 2010; Lenard et al., 2020). The main reason is that the mixing of sediment, eroded from catchments with different tectonic histories or at different stages in the accretion cycles, dilutes the tectonic signal. Besides, sediment reworking and transient storage in the floodplain, on the shelf, or within submarine canyons, as well as post-depositional reworking by physical and biological processes, and glacio-eustatic variations (e.g., Romans et al., 2016, and references therein) all contribute to further modifying the tectonic signals of any particular catchment. Therefore, ^{10}Be records from distal fans (such as the Bengal and Indus fans) may simply contain a spatially and temporally mixed signal.

Due to the lack of Yamuna-derived Quaternary sediment in the Haripur section, our erosion rate record is limited to between 6 and ~ 2 Ma. Thus the debate of whether or not Himalayan erosion rates have varied in concert with glacial-interglacial climate oscillations during the Quaternary remains open. Further high-resolution paleo-erosion rate studies using the last 2-Myr sedimentary archives of the proximal Himalayan foreland basin are needed to test the erosional response to short-term climatic oscillations during the Quaternary. The apparent transient response of erosion to putative basal accretion should be further tested in the future by applying this method to proximal foreland basin sediments stored in the stratigraphic record from other parts of the Himalaya and other orogens. The question of whether basal accretion-driven changes in topography and commensurate changes in erosion rates are otherwise expressed in the foreland basin stratigraphic record (i.e., the patterns documented in the sediment grain size record or provenance variation) should further be explored in future studies. However, the size-selective sorting (e.g., Ashworth & Ferguson, 1989), mechanical breakdown (abrasion) of particles en route to the foreland basin (e.g., Dingle et al., 2017), and internal river dynamics (e.g., Jerolmack & Paola, 2010) might result in dampening or destroying of environmental signals (e.g., Romans et al., 2016; Straub et al., 2020). Thus, the anticipated variation may not necessarily be expressed in the stratigraphic record. Lastly, the punctuated topographic growth in the internal part of the orogen and the commensurate change in accommodation space in the proximal alluvial foredeep should be a target of future studies to understand better the alluvial architecture of the late Cenozoic Himalayan foreland basin.

Appendix A: Landscape Evolution Modeling

The landscape evolution simulation was generated using the TopoToolbox Landscape Evolution Model (Campforts et al., 2017; Schwanghart & Scherler, 2014). This model implements the physics of tectonic displacement and river incision. Experiments were performed on a 40×40 km grid with a spatial resolution of 100 m and a time step of 10,000 years. The top, bottom, and right sides are no-flux boundaries, and the elevation is fixed at 0 m at the left boundary. Compared to the Himalayas, the left boundary can be thought of as the border between the mountain range and the Indo-Gangetic plain. River incision is based on the stream power model with $n = 1$ for the slope exponent, $m = 0.5$ for the area exponent, and $K = 4.0 \times 10^{-6}$ for the river incision efficiency. Hillslopes were simulated using linear hillslope diffusion with a value of $D = 10^{-3} \text{ m}^2 \text{ yr}^{-1}$ for the hillslope diffusivity. Because uplift rates in our experiment were rather high, hillslope degradation by diffusion is insufficient to keep pace with rock uplift. We, therefore, enabled a simple model for landslides that removes hillslope material, which stands above a critical threshold hillslope gradient (S_c) of 1 m m^{-1} (Blöthe et al., 2015). However, this approach generates oscillations in the erosion rates because the simulation produces landslides in one time step, whereas the next time step is free from any landslides. To circumvent this effect on the spatially integrated erosion rates, we applied zero-phase digital filtering to the erosion rate data.

The simulation was initialized by starting with a flat surface, sloping at 0.01° toward the left, and imposed random noise, which was subjected to a spatially uniform tectonic uplift rate of 1 mm yr^{-1} . After 2 Myr,

an approximately steady-state topography was established, and we changed the uplift pattern to simulate the effect of basal accretion and the presence of a mid-crustal ramp. The uplift pattern above the ramp was modeled as a strike-parallel, 10-km wide zone with an uplift rate of 5 mm yr^{-1} , five times greater than the background uplift rate that still affects all other areas. This choice of uplift rates is consistent with an expected rock uplift rate over the $\sim 16^\circ$ dipping mid-crustal ramp in the Main Himalayan Thrust (MHT), imaged by geophysical data in the Garhwal region (Caldwell et al., 2013), and assuming that the Himalayan wedge is sliding without any internal deformation over the ramp at an average rate of $\sim 18 \text{ mm yr}^{-1}$ (Stevens & Avouac, 2015). During cycles of basal accretion, we assume that the ramp in the MHT migrates with the downgoing plate at the speed of the underthrusting rate, until the ramp is abandoned and a new one is created farther to the south. We used $u_r = 10 \text{ mm yr}^{-1}$ for the rate at which the high uplift zone migrates through the catchment. After 2 Myr, the simulation continues for another 8 Myr. Thus, the model features four consecutive accretion cycles of equal magnitude, and each cycle has a period of 2 Myr.

The spatially averaged erosion rate, E , integrated over the time step length, was calculated using the following equation:

$$\frac{dE}{dt} = \frac{dU - dz}{dt} \quad (\text{A1})$$

The elevation difference for each time step, $\frac{dz}{dt}$, is obtained by subtracting the elevation grid in the previous time step from the updated, current elevation grid. U is the rock uplift rate. E refers to the actual erosion rates that result from all the surface processes within the computation domain. It varies spatially and temporally due to the migration of the high rock-uplift rate zone and the fact that the topography was not adjusted to the uplift field.

We also estimated erosion rates based on the expected ^{10}Be concentration in river sediment. The surface ^{10}Be concentration, C , was computed using the following equation (Lal, 1991):

$$C = \frac{P}{\lambda + \varepsilon \cdot \frac{\rho}{\Lambda}} \quad (\text{A2})$$

where ε and P are the erosion and production rate, respectively, of each cell of the model domain, λ is the ^{10}Be decay constant ($4.998 \pm 0.043 \times 10^{-7} \text{ yr}^{-1}$), ρ is the density of the eroded sediment (2.7 g cm^{-3}), Λ is the attenuation coefficient for the nucleonic component of the cosmic radiation (160 g cm^{-2}). For simplicity, we assumed that ^{10}Be production is entirely by spallation and neglected the minor (<2%) contribution from deeper-penetrating muons (Heisinger, Lal, Jull, Kubik, Ivy-Ochs, Knie, & Nolte, 2002; Heisinger, Lal, Jull, Kubik, Ivy-Ochs, Neumaier, et al., 2002), which has hardly an influence on the simulated ^{10}Be concentration. The average ^{10}Be concentration was computed by integrating sediment from all model domain cells, proportional to their erosion rates. This means that cells with a high erosion rate contribute more to the simulated river sediment than cells with a low-erosion rate. The simulated ^{10}Be concentration of river sediment was then used in conjunction with an average ^{10}Be production rate of the model domain to get an erosion rate. When the erosion rate of a specific time step was calculated using the ^{10}Be concentration and production rate from that time step, we get precisely the actual erosion rate (Equation A1). However, when we assume a constant production rate for the entire simulation period, as we do in our study of the Yamuna catchment, the two estimates disagree, and the amplitude of the cyclic erosion rate variations increases.

Conflict of Interest

The authors declare no conflicts of interest relevant to this study.

Data Availability Statement

Data Sets S1–S5 and Movie S1 are available from Mandal et al. (2021).

Acknowledgments

This research was supported by the Alexander von Humboldt Postdoctoral Fellowship, Science and Engineering Research Board, Department of Science and Technology, Government of India, grant SRG/2019/000005, and IISER Kolkata Start-up research grant IISER-K/DoRD/CRF/SKM/2018-19/504 to S.K. Mandal and German Science Foundation DFG-grant SCHE1676/3-1 to D. Scherler. The authors thank S. Binnie and S. Heinze for performing AMS measurements, R. Kapannusch for field support, J. Glodny, K. Martin, and C. Schulz for laboratory support, members of the GFZ Section 3.3 for discussions and suggestions, J.-P. Burg, J.-P. Avouac, J. Braun, and D. Burbank for comments and suggestions on an earlier version of the manuscript. Finally, the authors thank Mike Oskin, Peter Sadler, and two anonymous reviewers for their constructive comments.

References

- Adams, B. A., Whipple, K. X., Hodges, K. V., & Heimsath, A. M. (2016). In situ development of high-elevation, low-relief landscapes via duplex deformation in the Eastern Himalayan hinterland, Bhutan. *Journal of Geophysical Research: Earth Surface*, 121(2), 294–319. <https://doi.org/10.1002/2015jf003508>
- Ashworth, P. J., & Ferguson, R. I. (1989). Size-selective entrainment of bed load in gravel bed streams. *Water Resources Research*, 25(4), 627–634. <https://doi.org/10.1029/wr025i004p00627>
- Avouac, J.-P. (2015). Mountain building: From earthquakes to geologic deformation. In *Treatise on geophysics* (pp. 381–432). Elsevier. <https://doi.org/10.1016/b978-0-444-53802-4.00120-2>
- Barnes, J. B., Densmore, A. L., Mukul, M., Sinha, R., Jain, V., & Tandon, S. K. (2011). Interplay between faulting and base level in the development of Himalayan frontal fold topography. *Journal of Geophysical Research*, 116(F3). <https://doi.org/10.1029/2010jf001841>
- Beaumont, C., Jamieson, R. A., Nguyen, M. H., & Lee, B. (2001). Himalayan tectonics explained by extrusion of a low-viscosity crustal channel coupled to focused surface denudation. *Nature*, 414(6865), 738–742. <https://doi.org/10.1038/414738a>
- Berger, A. L., Gulick, S. P. S., Spotila, J. A., Upton, P., Jaeger, J. M., Chapman, J. B., et al. (2008). Quaternary tectonic response to intensified glacial erosion in an orogenic wedge. *Nature Geoscience*, 1(11), 793–799. <https://doi.org/10.1038/ngeo334>
- Bhattacharyya, K., & Mitra, G. (2009). A new kinematic evolutionary model for the growth of a duplex—An example from the Rangit duplex, Sikkim Himalaya, India. *Gondwana Research*, 16(3–4), 697–715. <https://doi.org/10.1016/j.gr.2009.07.006>
- Bierman, P., & Steig, E. J. (1996). Estimating rates of denudation using cosmogenic isotope abundances in sediment. *Earth Surface Processes and Landforms*, 21(2), 125–139. [https://doi.org/10.1002/\(sici\)1096-9837\(199602\)21:2<125::aid-esp511>3.0.co;2-8](https://doi.org/10.1002/(sici)1096-9837(199602)21:2<125::aid-esp511>3.0.co;2-8)
- Blöthe, J. H., Korup, O., & Schwanghart, W. (2015). Large landslides lie low: Excess topography in the Himalaya-Karakoram ranges. *Geology*, 43(6), 523–526. <https://doi.org/10.1130/g36527.1>
- Bollinger, L., Henry, P., & Avouac, J. (2006). Mountain building in the Nepal Himalaya: Thermal and kinematic model. *Earth and Planetary Science Letters*, 244(1–2), 58–71. <https://doi.org/10.1016/j.epsl.2006.01.045>
- Bookhagen, B., Thiede, R. C., & Strecker, M. R. (2005). Late Quaternary intensified monsoon phases control landscape evolution in the northwest Himalaya. *Geology*, 33(2), 149. <https://doi.org/10.1130/g20982.1>
- Braconnot, P. (2004). Modeling the last glacial maximum and mid-Holocene. *Comptes Rendus Geoscience*, 336(7), 711–719. <https://doi.org/10.1016/j.crte.2003.12.023>
- Braucher, R., Bourlès, D., Brown, E., Colin, F., Muller, J.-P., Braun, J.-J., et al. (2000). Application of in situ-produced cosmogenic ^{10}Be and ^{26}Al to the study of lateritic soil development in tropical forest: Theory and examples from Cameroon and Gabon. *Chemical Geology*, 170(1–4), 95–111. [https://doi.org/10.1016/s0009-2541\(99\)00243-0](https://doi.org/10.1016/s0009-2541(99)00243-0)
- Braucher, R., Brown, E., Bourlès, D., & Colin, F. (2003). In situ produced ^{10}Be measurements at great depths: Implications for production rates by fast muons. *Earth and Planetary Science Letters*, 211(3–4), 251–258. [https://doi.org/10.1016/s0012-821x\(03\)00205-x](https://doi.org/10.1016/s0012-821x(03)00205-x)
- Braucher, R., Merchel, S., Borgomano, J., & Bourlès, D. (2011). Production of cosmogenic radionuclides at great depth: A multi element approach. *Earth and Planetary Science Letters*, 309(1–2), 1–9. <https://doi.org/10.1016/j.epsl.2011.06.036>
- Braun, J., Voisin, C., Gourlan, A. T., & Chauvel, C. (2015). Erosional response of an actively uplifting mountain belt to cyclic rainfall variations. *Earth Surface Dynamics*, 3(1), 1–14. <https://doi.org/10.5194/esurf-3-1-2015>
- Brown, E. T., Stallard, R. F., Larsen, M. C., Raisbeck, G. M., & Yiou, F. (1995). Denudation rates determined from the accumulation of in situ-produced ^{10}Be in the Luquillo experimental forest, Puerto Rico. *Earth and Planetary Science Letters*, 129(1–4), 193–202. [https://doi.org/10.1016/0012-821x\(94\)00249-x](https://doi.org/10.1016/0012-821x(94)00249-x)
- Caldwell, W. B., Klemperer, S. L., Lawrence, J. F., Rai, S. S., & Ashish (2013). Characterizing the Main Himalayan Thrust in the Garhwal Himalaya, India with receiver function CCP stacking. *Earth and Planetary Science Letters*, 367, 15–27. <https://doi.org/10.1016/j.epsl.2013.02.009>
- Campforts, B., Schwanghart, W., & Govers, G. (2017). Accurate simulation of transient landscape evolution by eliminating numerical diffusion: The TTLEM 1.0 model. *Earth Surface Dynamics*, 5(1), 47–66. <https://doi.org/10.5194/esurf-5-47-2017>
- Catlos, E. J., Harrison, T. M., Kohn, M. J., Grove, M., Ryerson, F. J., Manning, C. E., & Upreti, B. N. (2001). Geochronologic and thermobarometric constraints on the evolution of the Main Central Thrust, central Nepal Himalaya. *Journal of Geophysical Research*, 106(B8), 16177–16204. <https://doi.org/10.1029/2000jb900375>
- Charreau, J., Blard, P.-H., Puchol, N., Avouac, J.-P., Lallier-Vergès, E., Bourlès, D., et al. (2011). Paleo-erosion rates in Central Asia since 9 Ma: A transient increase at the onset of quaternary glaciations? *Earth and Planetary Science Letters*, 304(1–2), 85–92. <https://doi.org/10.1016/j.epsl.2011.01.018>
- Chmeleff, J., von Blanckenburg, F., Kossett, K., & Jakob, D. (2010). Determination of the ^{10}Be half-life by multicollector ICP-MS and liquid scintillation counting. *Nuclear Instruments and Methods in Physics Research Section B: Beam Interactions with Materials and Atoms*, 268(2), 192–199. <https://doi.org/10.1016/j.nimb.2009.09.012>
- Clift, P. D., Hodges, K. V., Heslop, D., Hannigan, R., Long, H. V., & Calves, G. (2008). Correlation of Himalayan exhumation rates and Asian monsoon intensity. *Nature Geoscience*, 1(12), 875–880. <https://doi.org/10.1038/ngeo351>
- Colleps, C. L., McKenzie, N. R., Stockli, D. F., Hughes, N. C., Singh, B. P., Webb, A. A. G., et al. (2018). Zircon (U-Th)/He thermochronometric constraints on Himalayan Thrust belt exhumation, bedrock weathering, and cenozoic seawater chemistry. *Geochemistry, Geosystems*, 19(1), 257–271. <https://doi.org/10.1002/2017gc007191>
- Colleps, C. L., Stockli, D. F., McKenzie, N. R., Webb, A. A. G., & Horton, B. K. (2019). Neogene kinematic evolution and exhumation of the NW India Himalaya: Zircon geo- and thermochronometric insights from the fold-thrust belt and foreland basin. *Tectonics*, 38(6), 2059–2086. <https://doi.org/10.1029/2018tc005304>
- Crampton, J. S., Meyers, S. R., Cooper, R. A., Sadler, P. M., Foote, M., & Harte, D. (2018). Pacing of Paleozoic macroevolutionary rates by Milankovitch grand cycles. *Proceedings of the National Academy of Sciences*, 115(22), 5686–5691. <https://doi.org/10.1073/pnas.1714342115>
- Dahlen, F. A. (1990). Critical taper model of fold-and-thrust belts and accretionary wedges. *Annual Review of Earth and Planetary Sciences*, 18(1), 55–99. <https://doi.org/10.1146/annurev.ea.18.050190.000415>
- DeCelles, P. G., Carrapa, B., Gehrels, G. E., Chakraborty, T., & Ghosh, P. (2016). Along-strike continuity of structure, stratigraphy, and kinematic history in the Himalayan thrust belt: The view from Northeastern India. *Tectonics*, 35(12), 2995–3027. <https://doi.org/10.1002/2016tc004298>
- Dewald, A., Heinze, S., Jolie, J., Zilges, A., Dunai, T., Rethemeyer, J., et al. (2013). CologneAMS, a dedicated center for accelerator mass spectrometry in Germany. *Nuclear Instruments and Methods in Physics Research Section B: Beam Interactions with Materials and Atoms*, 294, 18–23. <https://doi.org/10.1016/j.nimb.2012.04.030>

- Dingle, E. H., Attal, M., & Sinclair, H. D. (2017). Abrasion-set limits on himalayan gravel flux. *Nature*, 544(7651), 471–474. <https://doi.org/10.1038/nature22039>
- Finnegan, N. J., Schumer, R., & Finnegan, S. (2014). A signature of transience in bedrock river incision rates over timescales of 104–107 years. *Nature*, 505(7483), 391–394. <https://doi.org/10.1038/nature12913>
- Gabet, E. J., Burbank, D. W., Pratt-Sitaula, B., Putkonen, J., & Bookhagen, B. (2008). Modern erosion rates in the High Himalayas of Nepal. *Earth and Planetary Science Letters*, 267(3–4), 482–494. <https://doi.org/10.1016/j.epsl.2007.11.059>
- Galy, V., France-Lanord, C., Beyssac, O., Faure, P., Kudrass, H., & Palhol, F. (2007). Efficient organic carbon burial in the Bengal fan sustained by the Himalayan erosional system. *Nature*, 450(7168), 407–410. <https://doi.org/10.1038/nature06273>
- Galy, V., France-Lanord, C., Peucker-Ehrenbrink, B., & Huyghe, P. (2010). Sr-Nd-Os evidence for a stable erosion regime in the Himalaya during the past 12 Myr. *Earth and Planetary Science Letters*, 290(3–4), 474–480. <https://doi.org/10.1016/j.epsl.2010.01.004>
- Ganti, V., von Hagke, C., Scherler, D., Lamb, M. P., Fischer, W. W., & Avouac, J.-P. (2016). Time scale bias in erosion rates of glaciated landscapes. *Science Advances*, 2(10), e1600204. <https://doi.org/10.1126/sciadv.1600204>
- Godard, V., Burbank, D. W., Bourlès, D. L., Bookhagen, B., Braucher, R., & Fisher, G. B. (2012). Impact of glacial erosion on ^{10}Be concentrations in fluvial sediments of the Marsyandi catchment, central Nepal. *Journal of Geophysical Research*, 117(F3). <https://doi.org/10.1029/2011jf002230>
- Goodbred, J., Steven, L., & Kuehl, S. A. (2000). Enormous Ganges-Brahmaputra sediment discharge during strengthened early Holocene monsoon. *Geology*, 28(12), 1083–1086. [https://doi.org/10.1130/0091-7613\(2000\)028<1083:egbsdd>2.3.co;2](https://doi.org/10.1130/0091-7613(2000)028<1083:egbsdd>2.3.co;2)
- Gourlan, A. T., Meynadier, L., Allègre, C. J., Tappognier, P., Birck, J.-L., & Joron, J.-L. (2010). Northern Hemisphere climate control of the Bengali rivers discharge during the past 4 Ma. *Quaternary Science Reviews*, 29(19–20), 2484–2498. <https://doi.org/10.1016/j.quascirev.2010.05.003>
- Gutscher, M.-A., Kukowski, N., Malavieille, J., & Lallemand, S. (1996). Cyclical behavior of thrust wedges: Insights from high basal friction sandbox experiments. *Geology*, 24(2), 135–138. [https://doi.org/10.1130/0091-7613\(1996\)024<0135:cbotwi>2.3.co;2](https://doi.org/10.1130/0091-7613(1996)024<0135:cbotwi>2.3.co;2)
- Harvey, J. E., Burbank, D. W., & Bookhagen, B. (2015). Along-strike changes in Himalayan thrust geometry: Topographic and tectonic discontinuities in western Nepal. *Lithosphere*, 7(5), 511–518. <https://doi.org/10.1130/l144.1>
- Heisinger, B., Lal, D., Jull, A., Kubik, P., Ivy-Ochs, S., Knie, K., & Nolte, E. (2002). Production of selected cosmogenic radionuclides by muons: 2. Capture of negative muons. *Earth and Planetary Science Letters*, 200(3–4), 357–369. [https://doi.org/10.1016/s0012-821x\(02\)00641-6](https://doi.org/10.1016/s0012-821x(02)00641-6)
- Heisinger, B., Lal, D., Jull, A., Kubik, P., Ivy-Ochs, S., Neumaier, S., et al. (2002). Production of selected cosmogenic radionuclides by muons: 1. fast muons. *Earth and Planetary Science Letters*, 200(3), 345–355. [https://doi.org/10.1016/S0012-821X\(02\)00640-4](https://doi.org/10.1016/S0012-821X(02)00640-4)
- Herman, F., Copeland, P., Avouac, J.-P., Bollinger, L., Mahéo, G., Fort, P. L., et al. (2010). Exhumation, crustal deformation, and thermal structure of the Nepal Himalaya derived from the inversion of thermochronological and thermobarometric data and modeling of the topography. *Journal of Geophysical Research*, 115(B6). <https://doi.org/10.1029/2008jb006126>
- Herman, F., Seward, D., Valla, P. G., Carter, A., Kohn, B., Willett, S. D., & Ehlers, T. A. (2013). Worldwide acceleration of mountain erosion under a cooling climate. *Nature*, 504(7480), 423–426. <https://doi.org/10.1038/nature12877>
- Jerolmack, D. J., & Paola, C. (2010). Shredding of environmental signals by sediment transport. *Geophysical Research Letters*, 37(19). <https://doi.org/10.1029/2010gl044638>
- Kapannusch, R., Scherler, D., King, G., & Wittmann, H. (2020). Glacial influence on late Pleistocene ^{10}Be -derived paleo-erosion rates in the north-western Himalaya, India. *Earth and Planetary Science Letters*, 547, 116441. <https://doi.org/10.1016/j.epsl.2020.116441>
- Kirby, E., & Whipple, K. X. (2012). Expression of active tectonics in erosional landscapes. *Journal of Structural Geology*, 44, 54–75. <https://doi.org/10.1016/j.jsg.2012.07.009>
- Kohn, M. J. (2014). Himalayan metamorphism and its tectonic implications. *Annual Review of Earth and Planetary Sciences*, 42(1), 381–419. <https://doi.org/10.1146/annurev-earth-060313-055005>
- Konstantinovskia, E., & Malavieille, J. (2005). Erosion and exhumation in accretionary orogens: Experimental and geological approaches. *Geochemistry, Geophysics, Geosystems*, 6(2). <https://doi.org/10.1029/2004gc000794>
- Korschinek, G., Bergmaier, A., Faestermann, T., Gerstmann, U., Knie, K., Rugel, G., et al. (2010). A new value for the half-life of ^{10}Be by Heavy-Ion Elastic Recoil Detection and liquid scintillation counting. *Nuclear Instruments and Methods in Physics Research Section B: Beam Interactions with Materials and Atoms*, 268(2), 187–191. <https://doi.org/10.1016/j.nimb.2009.09.020>
- Kumar, R., Ghosh, S. K., & Sangode, S. J. (1999). Evolution of a Neogene fluvial system in a Himalayan foreland basin, India. In *Himalaya and Tibet: Mountain roots to mountain tops*. Geological Society of America. <https://doi.org/10.1130/0-8137-2328-0.239>
- Lal, D. (1991). Cosmic ray labeling of erosion surfaces: In situ nuclide production rates and erosion models. *Earth and Planetary Science Letters*, 104(2–4), 424–439. [https://doi.org/10.1016/0012-821x\(91\)90220-c](https://doi.org/10.1016/0012-821x(91)90220-c)
- Lallier, F., Antoine, C., Charreau, J., Caumon, G., & Ruij, J. (2013). Management of ambiguities in magnetostratigraphic correlation. *Earth and Planetary Science Letters*, 371–372, 26–36. <https://doi.org/10.1016/j.epsl.2013.04.019>
- Lavé, J., & Avouac, J. P. (2000). Active folding of fluvial terraces across the Siwaliks Hills, Himalayas of central Nepal. *Journal of Geophysical Research*, 105(B3), 5735–5770. <https://doi.org/10.1029/1999jb90029>
- Lenard, S. J. P., Lavé, J., France-Lanord, C., Aumaître, G., Bourlès, D. L., & Keddadouche, K. (2020). Steady erosion rates in the Himalayas through late Cenozoic climatic changes. *Nature Geoscience*, 13(6), 448–452. <https://doi.org/10.1038/s41561-020-0585-2>
- Lifton, N., Sato, T., & Dunai, T. J. (2014). Scaling in situ cosmogenic nuclide production rates using analytical approximations to atmospheric cosmic-ray fluxes. *Earth and Planetary Science Letters*, 386, 149–160. <https://doi.org/10.1016/j.epsl.2013.10.052>
- Limpert, E., Stahel, W. A., & Abbt, M. (2001). Log-normal distributions across the sciences: Keys and clues. *BioScience*, 51, 341–352. [https://doi.org/10.1641/0006-3568\(2001\)051\[0341:LNDATS\]2.0.CO;2](https://doi.org/10.1641/0006-3568(2001)051[0341:LNDATS]2.0.CO;2)
- Lyon-Caen, H., & Molnar, P. (1985). Gravity anomalies, flexure of the Indian Plate, and the structure, support and evolution of the Himalaya and Ganga Basin. *Tectonics*, 4(6), 513–538. <https://doi.org/10.1029/tc004i006p00513>
- Madella, A., Delunel, R., Akçar, N., Schlunegger, F., & Christl, M. (2018). ^{10}Be -inferred paleo-denudation rates imply that the mid-Miocene western central Andes eroded as slowly as today. *Scientific Reports*, 8(1). <https://doi.org/10.1038/s41598-018-20681-x>
- Mandal, S., Robinson, D. M., Kohn, M. J., Khanal, S., & Das, O. (2019). Examining the tectono-stratigraphic architecture, structural geometry, and kinematic evolution of the Himalayan fold-thrust belt, Kumaun, northwest India. *Lithosphere*, 11(4), 414–435. <https://doi.org/10.1130/11050.1>
- Mandal, S. K., Scherler, D., Romer, R. L., Burg, J.-P., Guillong, M., & Schleicher, A. M. (2018). Multi-proxy isotopic and geochemical analysis of the Siwalik sediments in NW India: Implication for the Late Cenozoic tectonic evolution of the Himalaya. *Tectonics*. <https://doi.org/10.1029/2018tc005200>

- Mandal, S. K., Scherler, D., & Wittmann, H. (2021). Analysis of cosmogenic ^{10}Be concentrations of Siwalik sediments and modern river sands from the north-western Himalaya and the calculated ^{10}Be -derived paleoerosion rates. *GFZ Data Services*. <https://doi.org/10.5880/GFZ.3.3.2021.006>
- Mariotti, A., Blard, P.-H., Charreau, J., Toucanne, S., Jorry, S. J., Molliex, S., et al. (2021). Nonlinear forcing of climate on mountain denudation during glaciations. *Nature Geoscience*, 14(1), 16–22. <https://doi.org/10.1038/s41561-020-00672-2>
- Mehta, Y. P., Thakur, A. K., Lal, N., Shukla, B., & Tandon, S. K. (1993). Fission track age of zircon separates of tuffaceous mudstones of the Upper Siwalik subgroup of Jammu-Chandigarh sector of the Punjab Sub-Himalaya. *Current Science*, 64(7), 519–521.
- Menant, A., Angiboust, S., Gerya, T., Lacassin, R., Simoes, M., & Grandin, R. (2020). Transient stripping of subducting slabs controls periodic forearc uplift. *Nature Communications*, 11(1). <https://doi.org/10.1038/s41467-020-15580-7>
- Mendoza, M. M., Ghosh, A., Karplus, M. S., Klemperer, S. L., Sapkota, S. N., Adhikari, L. B., & Velasco, A. (2019). Duplex in the Main Himalayan Thrust illuminated by aftershocks of the 2015 Mw 7.8 Gorkha earthquake. *Nature Geoscience*, 12(12), 1018–1022. <https://doi.org/10.1038/s41561-019-0474-8>
- Mercier, J., Braun, J., & van der Beek, P. (2017). Do along-strike tectonic variations in the Nepal Himalaya reflect different stages in the accretion cycle? Insights from numerical modeling. *Earth and Planetary Science Letters*, 472, 299–308. <https://doi.org/10.1016/j.epsl.2017.04.041>
- Milliman, J. D., & Farnsworth, K. L. (2011). *River discharge to the coastal ocean: A global synthesis*. Cambridge University Press. <https://doi.org/10.1017/CBO9780511781247>
- Mishra, P., & Mukhopadhyay, D. K. (2012). Structural evolution of the frontal fold-thrust belt, NW Himalayas from sequential restoration of balanced cross-sections and its hydrocarbon potential. *Geological Society, London, Special Publications*, 366(1), 201–228. <https://doi.org/10.1144/sp366.6>
- Molnar, P. (2004). Late Cenozoic increase in accumulation rates of terrestrial sediment: How might climate change have affected erosion rates? *Annual Review of Earth and Planetary Sciences*, 32(1), 67–89. <https://doi.org/10.1146/annurev.earth.32.091003.143456>
- Molnar, P., & Stock, J. M. (2009). Slowing of India's convergence with Eurasia since 20 Ma and its implications for Tibetan mantle dynamics. *Tectonics*, 28(3). <https://doi.org/10.1029/2008TC002271>
- Mugnier, J.-L., & Huyghe, P. (2006). Ganges basin geometry records a pre-15 Ma isostatic rebound of Himalaya. *Geology*, 34(6), 445. <https://doi.org/10.1130/g22089.1>
- Najman, Y., Bickle, M., & Chapman, H. (2000). Early Himalayan exhumation: Isotopic constraints from the Indian foreland basin. *Terra Nova*, 12(1), 28–34. <https://doi.org/10.1046/j.1365-3121.2000.00268.x>
- Najman, Y., Jenks, D., Godin, L., Boudagher-Fadel, M., Millar, I., Garzanti, E., et al. (2017). The Tethyan Himalayan detrital record shows that India–Asia terminal collision occurred by 54 Ma in the Western Himalaya. *Earth and Planetary Science Letters*, 459, 301–310. <https://doi.org/10.1016/j.epsl.2016.11.036>
- Najman, Y., Johnson, K., White, N., & Oliver, G. (2004). Evolution of the Himalayan foreland basin, NW India. *Basin Research*, 16(1), 1–24. <https://doi.org/10.1111/j.1365-2117.2004.00223.x>
- Naylor, M., & Sinclair, H. (2007). Punctuated thrust deformation in the context of doubly vergent thrust wedges: Implications for the localization of uplift and exhumation. *Geology*, 35(6), 559. <https://doi.org/10.1130/g23448a.1>
- Nishizumi, K., Imamura, M., Caffee, M. W., Southon, J. R., Finkel, R. C., & McAninch, J. (2007). Absolute calibration of ^{10}Be AMS standards. *Nuclear Instruments and Methods in Physics Research Section B: Beam Interactions with Materials and Atoms*, 258(2), 403–413. <https://doi.org/10.1016/j.nimb.2007.01.297>
- Osokin, M. E., Longinotti, N. E., Peryam, T. C., Dorsey, R. J., DeBoer, C. J., Housen, B. A., & Blisniuk, K. D. (2017). Steady ^{10}Be -derived paleoerosion rates across the Plio-Pleistocene climate transition, Fish Creek–Vallecito basin, California. *Journal of Geophysical Research: Earth Surface*, 122(9), 1653–1677. <https://doi.org/10.1002/2016jf004113>
- Pälike, H., Norris, R. D., Herrle, J. O., Wilson, P. A., Coxall, H. K., Lear, C. H., et al. (2006). The heartbeat of the Oligocene climate system. *Science*, 314(5807), 1894–1898. <https://doi.org/10.1126/science.1133822>
- Peizhen, Z., Molnar, P., & Downs, W. R. (2001). Increased sedimentation rates and grain sizes 2–4 Myr ago due to the influence of climate change on erosion rates. *Nature*, 410(6831), 891–897. <https://doi.org/10.1038/35073504>
- Phillips, F. M., Argento, D. C., Balco, G., Caffee, M. W., Clem, J., Dunai, T. J., et al. (2016). The CRONUS-earth project: A synthesis. *Quaternary Geochronology*, 31, 119–154. <https://doi.org/10.1016/j.quageo.2015.09.006>
- Puchol, N., Charreau, J., Blard, P.-H., Lavé, J., Dominguez, S., Pik, R., & Saint-Carlier, D. (2016). Limited impact of quaternary glaciations on denudation rates in Central Asia. *Geological Society of America Bulletin*, 129(3–4), 479–499. <https://doi.org/10.1130/b31475.1>
- Ratschbacher, L., Frisch, W., Liu, G., & Chen, C. (1994). Distributed deformation in southern and western Tibet during and after the India–Asia collision. *Journal of Geophysical Research*, 99(B10), 19917–19945. <https://doi.org/10.1029/94jb00932>
- Raymo, M. E., & Ruddiman, W. F. (1992). Tectonic forcing of late Cenozoic climate. *Nature*, 359(6391), 117–122. <https://doi.org/10.1038/359117a0>
- Robert, X., van der Beek, P., Braun, J., Perry, C., & Mugnier, J.-L. (2011). Control of detachment geometry on lateral variations in exhumation rates in the Himalaya: Insights from low-temperature thermochronology and numerical modeling. *Journal of Geophysical Research*, 116(B5). <https://doi.org/10.1029/2010jb007893>
- Robinson, D. M., & Martin, A. J. (2014). Reconstructing the Greater Indian margin: A balanced cross section in central Nepal focusing on the Lesser Himalayan duplex. *Tectonics*, 33(11), 2143–2168. <https://doi.org/10.1002/2014tc003564>
- Romans, B. W., Castelltort, S., Covault, J. A., Fildani, A., & Walsh, J. (2016). Environmental signal propagation in sedimentary systems across timescales. *Earth-Science Reviews*, 153, 7–29. <https://doi.org/10.1016/j.earscirev.2015.07.012>
- Sadler, P. M. (1981). Sediment accumulation rates and the completeness of stratigraphic sections. *The Journal of Geology*, 89(5), 569–584. <https://doi.org/10.1080/628623>
- Sadler, P. M., & Jerolmack, D. J. (2014). Scaling laws for aggradation, denudation and progradation rates: The case for time-scale invariance at sediment sources and sinks. *Geological Society, London, Special Publications*, 404(1), 69–88. <https://doi.org/10.1144/sp404.7>
- Sangode, S. J., Kumar, R., & Ghosh, S. K. (1996). Magnetic polarity stratigraphy of the Siwalik sequence of Haripur area (HP), NW Himalaya. *Journal of the Geological Society of India*, 47, 683–704.
- Sangode, S. J., Kumar, R., & Ghosh, S. K. (2001). Application of magnetic fabric studies in an ancient fluvial sequence of NW Himalaya. *Current Science*, 81, 66–71.
- Sanyal, P., Bhattacharya, S., Kumar, R., Ghosh, S., & Sangode, S. (2004). Mio-Pliocene monsoonal record from Himalayan foreland basin (Indian Siwalik) and its relation to vegetational change. *Palaeogeography, Palaeoclimatology, Palaeoecology*, 205(1–2), 23–41. <https://doi.org/10.1016/j.palaeo.2003.11.013>

- Schaller, M., & Ehlers, T. (2006). Limits to quantifying climate driven changes in denudation rates with cosmogenic radionuclides. *Earth and Planetary Science Letters*, 248(1–2), 153–167. <https://doi.org/10.1016/j.epsl.2006.05.027>
- Schaller, M., von Blanckenburg, F., Hovius, N., Veldkamp, A., van den Berg, M. W., & Kubik, P. W. (2004). Paleoerosion rates from cosmogenic ^{10}Be in a 1.3 Ma terrace sequence: Response of the River Meuse to changes in climate and rock uplift. *The Journal of Geology*, 112(2), 127–144. <https://doi.org/10.1086/381654>
- Scherler, D., Bookhagen, B., & Strecker, M. R. (2014). Tectonic control on ^{10}Be -derived erosion rates in the Garhwal Himalaya, India. *Journal of Geophysical Research: Earth Surface*, 119(2), 83–105. <https://doi.org/10.1002/2013jf002955>
- Scherler, D., Bookhagen, B., Strecker, M. R., von Blanckenburg, F., & Rood, D. (2010). Timing and extent of late Quaternary glaciation in the western Himalaya constrained by ^{10}Be moraine dating in Garhwal, India. *Quaternary Science Reviews*, 29(7–8), 815–831. <https://doi.org/10.1016/j.quascirev.2009.11.031>
- Scherler, D., Bookhagen, B., Wulf, H., Preusser, F., & Strecker, M. R. (2015). Increased late Pleistocene erosion rates during fluvial aggradation in the Garhwal Himalaya, northern India. *Earth and Planetary Science Letters*, 428, 255–266. <https://doi.org/10.1016/j.epsl.2015.06.034>
- Schildgen, T. F., van der Beek, P. A., Sinclair, H. D., & Thiede, R. C. (2018). Spatial correlation bias in late-cenozoic erosion histories derived from thermochronology. *Nature*, 559(7712), 89–93. <https://doi.org/10.1038/s41586-018-0260-6>
- Schwanghart, W., & Scherler, D. (2014). Short communication: TopoToolbox 2—MATLAB-based software for topographic analysis and modeling in earth surface sciences. *Earth Surface Dynamics*, 2(1), 1–7. <https://doi.org/10.5194/esurf-2-1-2014>
- Sinha, R., Friend, P. F., & Switsur, V. R. (1996). Radiocarbon dating and sedimentation rates in the Holocene alluvial sediments of the northern Bihar plains, India. *Geological Magazine*, 133(1), 85–90. <https://doi.org/10.1017/s0016756800007263>
- Sobel, E. R., Hilly, G. E., & Strecker, M. R. (2003). Formation of internally drained contractional basins by aridity-limited bedrock incision. *Journal of Geophysical Research*, 108(B7). <https://doi.org/10.1029/2002jb001883>
- Srivastava, P., & Mitra, G. (1994). Thrust geometries and deep structure of the outer and lesser Himalaya, Kumaon and Garhwal (India): Implications for evolution of the Himalayan fold-and-thrust belt. *Tectonics*, 13(1), 89–109. <https://doi.org/10.1029/93tc01130>
- Stevens, V. L., & Avouac, J. P. (2015). Interseismic coupling on the Main Himalayan Thrust. *Geophysical Research Letters*, 42(14), 5828–5837. <https://doi.org/10.1002/2015gl064845>
- Stolar, D. B., Willett, S. D., & Roe, G. H. (2006). Climatic and tectonic forcing of a critical orogen. In *Tectonics, climate, and landscape evolution*. Geological Society of America. [https://doi.org/10.1130/2006.2398\(14\)](https://doi.org/10.1130/2006.2398(14))
- Straub, K. M., Duller, R. A., Foreman, B. Z., & Hajek, E. A. (2020). Buffered, incomplete, and shredded: The challenges of reading an imperfect stratigraphic record. *Journal of Geophysical Research: Earth Surface*, 125(3). <https://doi.org/10.1029/2019jf005079>
- Tamrakar, N. K., Yokota, S., & Nakamura, M. (1999). Some mechanical properties of the Siwalik sandstones and their relation to petrographic properties. *Shimane University Global Resources and Environmental Studies Research Report*, 18, 41–54. [https://doi.org/10.1016/s0026-0657\(99\)80237-9](https://doi.org/10.1016/s0026-0657(99)80237-9)
- Tripathi, J. K., Bock, B., & Rajamani, V. (2013). Nd and Sr isotope characteristics of Quaternary Indo-Gangetic plain sediments: Source distinctiveness in different geographic regions and its geological significance. *Chemical Geology*, 344, 12–22. <https://doi.org/10.1016/j.chemgeo.2013.02.016>
- Val, P., & Hoke, G. D. (2016). A practical tool for examining paleoerosion rates from sedimentary deposits using cosmogenic radio nuclides: Examples from hypothetical scenarios and data. *Geochemistry, Geophysics, Geosystems*, 17(12), 5078–5088. <https://doi.org/10.1002/2016gc006608>
- Val, P., Hoke, G. D., Fosdick, J. C., & Wittmann, H. (2016). Reconciling tectonic shortening, sedimentation and spatial patterns of erosion from ^{10}Be paleo-erosion rates in the Argentine Precordillera. *Earth and Planetary Science Letters*, 450, 173–185. <https://doi.org/10.1016/j.epsl.2016.06.015>
- Valla, P. G., Shuster, D. L., & van der Beek, P. A. (2011). Significant increase in relief of the European Alps during mid-Pleistocene glaciations. *Nature Geoscience*, 4(10), 688–692. <https://doi.org/10.1038/ngeo1242>
- Vannay, J.-C., Grasemann, B., Rahn, M., Frank, W., Carter, A., Baudraz, V., & Cosca, M. (2004). Miocene to Holocene exhumation of metamorphic crustal wedges in the NW Himalaya: Evidence for tectonic extrusion coupled to fluvial erosion. *Tectonics*, 23(1). <https://doi.org/10.1029/2002tc001429>
- von Blanckenburg, F. (2006). The control mechanisms of erosion and weathering at basin scale from cosmogenic nuclides in river sediment. *Earth and Planetary Science Letters*, 242(3–4), 224–239. <https://doi.org/10.1016/j.epsl.2005.11.017>
- von Blanckenburg, F., Belshaw, N., & O’Nions, R. (1996). Separation of ^9Be and cosmogenic ^{10}Be from environmental materials and SIMS isotope dilution analysis. *Chemical Geology*, 129(1–2), 93–99. [https://doi.org/10.1016/0009-2541\(95\)00157-3](https://doi.org/10.1016/0009-2541(95)00157-3)
- von Blanckenburg, F., Bouchez, J., Ibarra, D. E., & Maher, K. (2015). Stable runoff and weathering fluxes into the oceans over Quaternary climate cycles. *Nature Geoscience*, 8(7), 538–542. <https://doi.org/10.1038/ngeo2452>
- Wang, H., Lu, H., Zhao, L., Zhang, H., Lei, F., & Wang, Y. (2019). Asian monsoon rainfall variation during the Pliocene forced by global temperature change. *Nature Communications*, 10(1). <https://doi.org/10.1038/s41467-019-13338-4>
- Wang, Y., Cheng, H., Edwards, R. L., Kong, X., Shao, X., Chen, S., et al. (2008). Millennial- and orbital-scale changes in the East Asian monsoon over the past 224,000 years. *Nature*, 451(7182), 1090–1093. <https://doi.org/10.1038/nature06692>
- Webb, A. A. G. (2013). Preliminary balanced palinspastic reconstruction of Cenozoic deformation across the Himachal Himalaya (northwestern India). *Geosphere*, 9(3), 572–587. <https://doi.org/10.1130/GES00787.1>
- Webb, A. A. G., Yin, A., Harrison, T. M., Célérrier, J., Gehrels, G. E., Manning, C. E., & Grove, M. (2011). Cenozoic tectonic history of the Himachal Himalaya (northwestern India) and its constraints on the formation mechanism of the Himalayan orogen. *Geosphere*, 7(4), 1013–1061. <https://doi.org/10.1130/GES00627.1>
- Wells, N. A., & Dorr, J. A. (1987). Shifting of the Kosi River, northern India. *Geology*, 15(3), 204–207. [https://doi.org/10.1130/0091-7613\(1987\)15<204:sotkrn>2.0.co;2](https://doi.org/10.1130/0091-7613(1987)15<204:sotkrn>2.0.co;2)
- Wesnousky, S. G., Kumar, S., Mohindra, R., & Thakur, V. C. (1999). Uplift and convergence along the Himalayan Frontal Thrust of India. *Tectonics*, 18(6), 967–976. <https://doi.org/10.1029/1999tc900026>
- Whipple, K. X. (2009). The influence of climate on the tectonic evolution of mountain belts. *Nature Geoscience*, 2(2), 97–104. <https://doi.org/10.1038/ngeo413>
- Whipple, K. X., & Meade, B. (2006). Orogen response to changes in climatic and tectonic forcing. *Earth and Planetary Science Letters*, 243(1–2), 218–228. <https://doi.org/10.1016/j.epsl.2005.12.022>
- Willenbring, J. K., & von Blanckenburg, F. (2010). Long-term stability of global erosion rates and weathering during late-cenozoic cooling. *Nature*, 465(7295), 211–214. <https://doi.org/10.1038/nature09044>

- Willett, S. D., Herman, F., Fox, M., Stalder, N., Ehlers, T. A., Jiao, R., & Yang, R. (2020). Bias and error in modelling thermochronometric data: Resolving a potential increase in Plio-Pleistocene erosion rate. *Earth Surface Dynamics*. <https://doi.org/10.5194/esurf-2020-59>
- Willett, S. D., Schlunegger, F., & Picotti, V. (2006). Messinian climate change and erosional destruction of the central European Alps. *Geology*, 34(8), 613. <https://doi.org/10.1130/g22280.1>
- Wittmann, H., Oelze, M., Gaillardet, J., Garzanti, E., & von Blanckenburg, F. (2020). A global rate of denudation from cosmogenic nuclides in the earth's largest rivers. *Earth-Science Reviews*, 204, 103147. <https://doi.org/10.1016/j.earscirev.2020.103147>
- Zachos, J. (2001). Trends, rhythms, and aberrations in global climate 65 Ma to present. *Science*, 292(5517), 686–693. <https://doi.org/10.1126/science.1059412>
- Zilio, L. D., Ruh, J., & Avouac, J.-P. (2020). Structural evolution of orogenic wedges: Interplay between erosion and weak décollements. *Tectonics*, 39(10). <https://doi.org/10.1029/2020tc006210>